Jet launching from binary neutron star mergers: Incorporating neutrino transport and magnetic fields

Lunan Sun, ^{1,*} Milton Ruiz⁰, ¹ Stuart L. Shapiro⁰, ^{1,2} and Antonios Tsokaros ¹ Department of Physics, University of Illinois at Urbana-Champaign, Urbana, Illinois 61801, USA ² Department of Astronomy and NCSA, University of Illinois at Urbana-Champaign, Urbana, Illinois 61801, USA

(Received 24 February 2022; accepted 18 April 2022; published 16 May 2022)

We perform general relativistic, magnetohydrodynamic simulations of merging binary neutron stars incorporating neutrino transport and magnetic fields. Our new radiative transport module for neutrinos adopts a general relativistic, truncated-moment formalism. The binaries consist of two identical, irrotational stars modeled by the Skyrme Lyon (SLy) nuclear equation of state. They are initially in quasicircular orbit and threaded with a poloidal magnetic field that extends from the stellar interior into the exterior, as in typical pulsars. We insert neutrino processes shortly after the merger and focus on the role of neutrinos in launching a jet following the collapse of the hypermassive neutron star (HMNS) remnant to a spinning black hole (BH). We treat two microphysical versions: one (a "warm-up") evolving a single neutrino species and considering only charged-current processes and the other evolving three species $(\nu_e, \bar{\nu}_e, \nu_x)$ and related processes. We trace the evolution until the system reaches a quasiequilibrium state after BH formation. We find that the BH + disk remnant eventually launches an incipient jet. The electromagnetic Poynting luminosity is $\sim 10^{53}$ erg s⁻¹, consistent with that of typical short gamma-ray bursts. The effect of neutrino cooling shortens the lifetime of the HMNS and lowers the amplitude of the major peak of the gravitational wave power spectrum somewhat. After BH formation, neutrinos help clear out the matter near the BH poles, resulting in lower baryon-loaded surrounding debris. The neutrino luminosity resides in the range $\sim 10^{52-53}$ erg s⁻¹ once quasiequilibrium is achieved. Comparing with the neutrino-free models, we observe that the inclusion of neutrinos yields similar ejecta masses and is inefficient in carrying off additional angular momentum.

DOI: 10.1103/PhysRevD.105.104028

I. INTRODUCTION

The coincident detection of gravitational waves (GWs) and electromagnetic (EM) signals from the first established neutron star binary (NSNS) merger GW170817 [1-7] provides a unique opportunity to study systematically the properties of compact objects, nuclear physics, and electromagnetism in strong gravity. The simultaneous detection of GW and EM signals from the NSNS mergers is the prime target of multimessenger astronomy and can provide us with important information about high-energy astrophysics phenomena in strong gravity, the synthesis of heavy nuclei, the properties of dense, nuclear matter, etc. In particular, the observation of GW170817 coincident with the short gamma-ray burst (sGRB) GRB170817A [8] demonstrated that NSNS remnants can power sGRBs [1,9,10]. In addition, this GW observation and its association with kilonova AT 2017gfo/DLT17ck [11] indicate that, in contrast to black hole (BH) binary mergers, compact binary mergers where at least one of the

companions is a neutron star (NS) are likely to be followed by various processes involving electromagnetic and neutrino emission. To systematically interpret multimessenger signals and their relation to the properties of the binary system, it is necessary to perform full general relativistic, magnetohydrodynamic (GRMHD) simulations incorporating detailed microphysical processes.

It has been long established that magnetic fields play a critical role in the fate of NSNS merger remnants. The Kelvin-Helmholtz instability (KHI) at the contact surface once the NSs touch for the first time triggers the exponential amplification of the magnetic field strength [12–15]. Subsequently, material is ejected due to orbital angular momentum advection and to torques [16,17]. There has been a series of systematic numerical studies of the effect of magnetic fields on NSNS mergers (see, e.g., Refs. [15,18–30] and references therein). In particular, we have shown that NSNS remnants consisting of a BH + disk can launch a collimated, mildly relativistic outflow—an incipient jet—with duration and luminosity consistent with typical sGRB central engine lifetimes and magnitudes, as well as with the Blandford-Znajek mechanism [31] (hereafter BZ) for

lsun11@illinois.edu

launching jets and their associated Poynting luminosities [26,32]. We also reported that a jet is launched following the delayed collapse of a hypermassive neutron star (HMNS) remnant if the initial pulsarlike magnetic field (i.e., magnetic filed that extends from the neutron star interior into its exterior) in the binary companions has a sufficiently large-scale poloidal component aligned to the orbital angular momentum of the system. The simulations in Ref. [33] suggest that this initial poloidal component is needed to amplify the magnetic energy to $\gtrsim 10^{50}$ erg in the BH + disk remnant, a threshold value that is required for jet launching. It is worth emphasizing that the emergence of a jet does not require relying on the development of a largescale poloidal magnetic field component in the HMNS, but only initially, as in typical pulsars, which is what we reported in Ref. [26]. In addition, our GRMHD simulations of merging black hole-neutron star (BHNS) binaries, where the NS is endowed with a magnetic field that extends from the stellar interior into the exterior, show that a jet may be launched from the highly spinning BH + disk remnant if the initial BH spin satisfies $a/M_{\rm BH} \gtrsim 0.4$ and an approximate alignment of the magnetic moment with the total angular momentum of the system is present [32,34].

Neutrino processes (e.g., cooling and emission) may also have significant effects on the fate of NSNS merger remnants. It has been suggested that neutrino pair annihilation could carry a large amount of energy from the inner region of the disk [35-38]. The thinning of the disk may result in a favorable geometry for jet launching [28,35], though the duration and energy of neutrino emission in NSNS mergers are likely to be insufficient for the outflows to break out from the ejecta shell and form relativistic jets [38]. It is also believed that neutrino-driven winds, in which neutrinos absorbed in the disk can lift matter out of its gravitational potential, are a crucial mechanism of mass loss for NSNS mergers [39–42]. Moreover, it was recently suggested that the jet launching mechanism could be a joint process of two widely accepted GRB central engine models: a BH model, where a stellar-mass BH is surrounded by a neutrino cooling-dominated accretion flow first proposed in Ref. [35], and the BZ mechanism [31], where the BH rotational energy is extracted by the magnetic field. According to Ref. [43], an initially nonspinning BH may first launch a thermal "fireball" via neutrino annihilation, followed by a more powerful, Poynting-flux dominated jet via the BZ process once the BH is spun up by accretion. Neutrinos may also have important effects on the magnetorotational instability (MRI), which is one of the main mechanisms to amplify the magnetic field to the strength required for jet launching (typically $\gtrsim 10^{15}$ G; see, e.g., Ref. [44]). As the joint contribution and interaction between neutrino transfer and magnetic fields may produce copious interesting effects in compact binary mergers, numerical simulations of mergers with full global and microphysical ingredients are crucial in determining the real physics of the jet-launching mechanism underlying recent observations, such as GRB 170817A and GRB 160625B [8,45].

Neutrino transport schemes in compact binary simulations have been developed and improved somewhat slowly. This is mainly because of long-standing complications with numerically solving Boltzmann's equation of radiation transport, whose requirement of evolving a system in six-dimensional phase space plus time for each species of neutrinos makes its application computationally expensive and impractical. Moreover, the interaction timescale between matter and radiation is shorter than the dynamical timescale of magnetohydrodynamics (MHD) matter in optically thick regions, making the numerical simulation more challenging to perform with sufficient resolution. To achieve neutrino transport in compact binary merger systems, simplifications of the exact transport equations have been applied. These include the simplest leakage schemes, which are based on the assumption that the neutrino diffusion timescale is much longer than the weak interaction timescale [46,47]. With a leakage scheme, one can trace the approximate local energy variation of neutrinos and neutrino cooling but cannot treat nonlocal neutrino-matter interactions and neutrino heating. More sophisticated are truncated moment formalisms, in particular, the two-moment (M1) scheme with analytic closure [48–51], and a mixed leakage—one moment scheme [52] for evolving binary merger systems. Recently, an improved M1 scheme was proposed in Ref. [53] and evolves the neutrino number density and yields a local estimate of the average neutrino energy. It shows that the composition of the polar ejecta in a NSNS merger is less neutron rich than in their previous simulations, where the neutrino spectrum was assumed to be energy independent in optically thin regions. More recently, a general relativistic Monte Carlo (MC) scheme has been implemented for the simulation of an unequal-mass NSNS merger [54,55]. This has shown that MC and M1 have similar and consistent outcomes of ejected material and neutrino outflow, except for a factor of ~2 difference in the luminosity of heavy-lepton neutrinos. However, the studies above are purely hydrodynamic simulations and do not study the joint effect of neutrino radiation and magnetic fields.

A recent GRMHD study of the NSNS postmerger phase that includes a neutrino leakage scheme, in which the remnant is seeded with a poloidal magnetic field 17 ms after merger, reports that the strong toroidal field ($\sim 10^{16}$ G) around a HMNS remnant is able to launch a magnetically driven outflow [56]. Neutrino cooling may help to reduce the baryon load in the polar region above the HMNS. However, the maximum attainable Lorentz factor in these simulations ($\Gamma_L \lesssim 5$) is too low to explain most sGRBs [57]. It is also claimed that, with a better neutrino evolution scheme that includes pair annihilation and radiative

processes, the Lorentz factor could be boosted to higher values. Therefore, a numerical GRMHD study of NSNS merger with a neutrino transport scheme that includes key interactions would provide new information regarding the merger remnant, radiation signals, jet-launching mechanism, and many other important features. More recently, a GRMHD simulation of a BHNS merger with neutrino transfer using a combined leakage-moment method has been performed in Ref. [58]. It finds that during the merger dynamical mass ejection and accretion disk formation occur shortly after tidal disruption. The magnetic field is strengthened due to magnetic winding and MRI. Moreover, postmerger mass ejection due to magnetically induced turbulent viscosity takes place ~300–500 ms after the tidal disruption, with the neutrino luminosity dropping quickly below $\sim 10^{51}$ erg s⁻¹. It also claims that a high-intensity Poynting flux is generated a few hundred ms after merger and remains strong for 1-2 s, which agrees with the duration of typical sGRBs.

In this work, we perform GRMHD simulations of NSNS mergers modeled using a piecewise polytropic representation of the nuclear SLy nuclear equation of state (EOS) [59] and initially endowed with a poloidal magnetic field extending from the stellar interior to the exterior, as in pulsars. Shortly after merger, we insert neutrino transfer using an M1 closure scheme. We performed two versions: (i) a simplified "warm-up" version involving only one neutrino species $(\bar{\nu}_e)$ and considering only charged-current interactions (called "Rad-Simp") and (ii) a full, more realistic version that evolves three neutrino species and considers additional microphysical processes ("Rad-Full"). We compare our results to simulations that include neither magnetic fields nor neutrino transport ("Unmag") as well as those that include only magnetic fields ("Mag") and those that include only neutrinos transport ("Unmag + Rad").

We find that neutrino processes enhance the angular momentum transport accelerating the collapse of the HMNS. As a consequence, in neutrino transport cases, the GW waveform is shorter in duration, though its strain amplitude remains above the sensitivity curve of next generation GW observatories, such as the Einstein Telescope (ET), between 1 and 5 kHz, assuming a source distance of 50 Mpc. We note that the most prominent peak in the strain may be detectable by aLIGO and A^+ as well. We also find that neutrinos do not have significant impact on the growth of the magnetic field, but they have the effect of clearing out the polar region above the BH poles, inducing a lower baryon load in surrounding debris. A magnetically driven jet is launched after $\gtrsim 10$ ms following the collapse of the HMNS. However, the delay time between the peak GW (i.e., the binary merger) and the emergence of the jet is significantly shorter in neutrino radiation cases. The outgoing EM Poynting luminosity $[L_{\rm EM} \sim 10^{53}~{\rm erg~s^{-1}}]$ is roughly consistent with sGRB models [60–62] and the luminosity associated with the BZ mechanism [31].

A key motivation of our project has been to implement a neutrino transport scheme into our Illinois GRMHD code, which has been used successfully to treat compact binary mergers (see, e.g., Refs. [63–68], including those involving magnetized neutron stars [33,69]). While the M1 scheme we adopt is not the most advanced and the results we report here are not likely the final answers, they are sufficient to generate a preliminary sketch of the combined influence of magnetic fields and neutrino transport on compact binary mergers and other astrophysical scenarios in strong gravitational fields.

The structure of the paper is summarized as follows. In Sec. II, we introduce our implementation of M1 radiation transport and the microphysical interactions responsible for thermal neutrino emission. A more detailed description and a strong-field test of our M1 scheme are presented in Appendices A–F. We next describe our adopted numerical setup and initial conditions in Sec. III. We discuss the effects of the magnetic field and thermal neutrino emission on the nature of the merger, properties of the remnant and ejecta, and the strength and detectability of GW and EM signals in Sec. IV. Finally, we summarize our findings and identify some limitations of our simulations in Sec. V. Throughout the paper, we adopt geometrized units (G = c = 1) except where stated otherwise. Greek indices denote all four spacetime dimensions, while latin indices imply spatial parts only.

II. FORMALISM AND METHOD

A. Numerical methods

The simulations in this work are performed using the original Illinois GRMHD code [70], coupled with our newly developed neutrino radiation moment formalism and transport module. The code is embedded in the CACTUS infrastructure [71] using CARPET as the moving-mesh refinement scheme [72]. The code evolves the Baumgarte-Shapiro-Shibata-Nakamura (BSSN) gravitational field equations [73,74] coupled to the moving puncture gauge conditions [75,76], using fourth-order centered spatial differencing, except on shift advection terms, where a fourth-order upwind differencing is used. In all our evolution cases, we set the damping coefficient η_{β} appearing in the shift condition to 2.7/M, where M is the Arnowitt-Deser-Misner (ADM) mass of the system. The BSSN evolution equations are embedded with fifth-order Kreiss-Oliger dissipation [77]. We also adopt the generalized Lorenz gauge [78,79] to evolve Maxwell's equations and employ a damping parameter $\zeta = 4.1/M$ to avoid the rise of spurious magnetic fields due to interpolations across refinement levels (see Ref. [78] for details). Time integration is performed using the method of lines with a fourth-order Runge-Kutta integration scheme with a Courant-Friedrichs-Lewy factor of 0.5. In the absence of neutrinos, this code has been thoroughly tested and used in the past in various scenarios involving compact binaries (e.g., Refs. [33,63–69]). The incorporation of radiation in the optically thick limit was previously used and tested in Ref. [80]. For implementation details, see Refs. [70,79–81].

B. Evolution of radiation fields

1. Radiation fields: M1 transport

We adopt and generalize the radiation transport approach described in Ref. [80], in which a basic radiation transport scheme applicable for optically thick gases was embedded in the Illinois GRMHD code. The local properties of the radiation can be described by the specific intensity $I_{\nu} = I(x^{\mu}; N^{i}; \nu)$, where x^{μ} is the coordinate position, N^{i} is the direction of radiation, and ν is the frequency with $N^{\mu} = p^{\mu}/(h\nu)$, with p^{μ} the 4-momentum of the photon and h the Planck constant. The quantities above are measured in the local Lorentz frame of a fiducial observer. The evolution of I_{ν} can be described by the Boltzmann equation for radiation transport, which is a 6 + 1-dimensional integrodifferential equation system whose numerical integration requires extremely large computational resources. To realize the numerical evolution of radiation fields, several approximations need to be imposed. First, we adopt the moment formalism (see, e.g., Ref. [82]) and consider the three lowest moments. We use the energy-(frequency-)integrated equations and the energy-averaged emissivities and opacities. For an observer comoving with the fluid, the energy moments of interest are the radiation energy density,

$$E = \int d\nu d\Omega I_{\nu},\tag{1}$$

the radiation flux,

$$F^{\alpha}=h^{\alpha}_{\ \gamma}\int d\nu d\Omega I_{\nu}N^{\gamma}; \eqno(2)$$

and the radiation stress tensor,

$$\mathcal{P}^{\alpha\beta} = h^{\alpha}_{\ \gamma} h^{\beta}_{\ \delta} \int d\nu d\Omega I_{\nu} N^{\gamma} N^{\delta}, \qquad (3)$$

where $d\Omega$ is the solid angle measured in the local Lorentz frame and $h^{\alpha\beta}=g^{\alpha\beta}+u^\alpha u^\beta$ is the projection tensor onto the orthogonal slices of the fluid 4-velocity u^α . We note that F^α is orthogonal to the fluid 4-velocity. With the above expressions, one can decompose the radiation tensor in terms of an observer comoving with the fluid as

$$R^{\alpha\beta} = Eu^{\alpha}u^{\beta} + F^{\alpha}u^{\beta} + F^{\beta}u^{\alpha} + \mathcal{P}^{\alpha\beta}. \tag{4}$$

In the numerical evolution, the highest-order radiation moments, E and F^i , are used as the primitive variables for the radiation (neutrino) fields. We then obtain F^0 using $F^\alpha u_\alpha = 0$, where u^α satisfies $u^\alpha u_\alpha = -1$ with $u^\mu = (u^0,0)$. The radiation stress tensor $\mathcal{P}^{\alpha\beta}$ is computed as a function of E and F^α according to the Minerbo closure scheme [83], which is an interpolation between the analytical expressions in optically thick and thin limits (see Appendix A). At each time step, the primitive variables are computed from the conserved variables, which are related to quantities measured by normal observers (see below) using a four-dimensional (4D) Newton-Rasphson solver described in Appendix B.

One can also decompose the radiation stress-energy tensor according to the normal observer

$$R^{\alpha\beta} = \bar{E}n^{\alpha}n^{\beta} + \bar{F}^{\alpha}n^{\beta} + \bar{F}^{\beta}n^{\alpha} + \bar{\mathcal{P}}^{\alpha\beta}, \tag{5}$$

where n^{α} is the unit vector normal to the constant t slice. The barred quantities,

$$\bar{E} = n_{\alpha} n_{\beta} R^{\alpha\beta} = \alpha^2 R^{00}, \tag{6}$$

$$\bar{F}^{\alpha} = -\gamma^{\alpha}{}_{\rho} n_{\beta} R^{\beta \rho} = \alpha (R^{\alpha 0} + \beta^{\alpha} R^{00}), \tag{7}$$

$$\bar{\mathcal{P}}^{\alpha\beta} = \gamma^{\alpha}_{\ \rho} \gamma^{\beta}_{\ \sigma} R^{\rho\sigma} = R^{\alpha\beta} - \alpha (n^{\alpha} R^{\beta 0} + n^{\beta} R^{\alpha 0}) + \alpha^2 n^{\alpha} n^{\beta} R^{00}, \tag{8}$$

are the radiation energy density, flux, and stress tensor with respect to a normal observer, respectively. Here, $\gamma^{\alpha\beta}=g^{\alpha\beta}+n^{\alpha}n^{\beta}$ is the projection operator onto slices of constant t, and α and β^{μ} are the lapse and shift functions, respectively. Note that Eqs. (6)–(8) can also be regarded as the purely normal, mixed normal-spatial, and purely spatial components of $R^{\alpha\beta}$, respectively [84]. They are directly related to the conserved radiation variables for the radiation dynamical equations (see Sec. II B 2). The conversion between the fluid-frame variables and the normal-frame variables is given by Refs. [84,85],

$$\bar{E} = W^2 E + 2W v_{\alpha} \bar{F}^{\alpha} + v_{\alpha} v_{\beta} \bar{\mathcal{P}}^{\alpha\beta}, \tag{9}$$

$$\begin{split} \bar{F}_{\alpha} &= W^2 v_{\alpha} E + W (g_{\alpha\beta} - n_{\alpha} n_{\beta}) F^{\beta} \\ &+ W v_{\alpha} v_{\beta} F^{\beta} + W (g_{\alpha\beta} - n_{\alpha} n_{\beta}) v_{\gamma} \mathcal{P}^{\beta\gamma}, \end{split} \tag{10}$$

$$\begin{split} \bar{\mathcal{P}}_{\alpha\beta} &= W^2 v_{\alpha} v_{\beta} E + W (g_{\alpha\gamma} - n_{\alpha} n_{\gamma}) v_{\beta} F^{\gamma} \\ &+ W (g_{\gamma\beta} - n_{\gamma} n_{\beta}) v_{\alpha} F^{\gamma} \\ &+ (g_{\alpha\gamma} - n_{\alpha} n_{\gamma}) (g_{\beta\delta} - n_{\beta} n_{\delta}) \mathcal{P}^{\gamma\delta}, \end{split} \tag{11}$$

where the 4-velocity is decomposed into its orthogonal and tangent parts

$$u^{\alpha} = W(n^{\alpha} + v^{\alpha}), \tag{12}$$

TABLE I. Comparison of the two microphysics versions employed here.

Microphysics scheme	Simplified	Full
\overline{Y}_e	0	Evolved
$\overline{Y_p}$	0	Y_e
$\overline{Y_n}$	1	$1-Y_e$
Emission:		
$e^+ + n \rightarrow p + \bar{\nu}_e$	✓	✓
$e^- + p \rightarrow n + \nu_e$	X	✓
$e^- + e^+ \rightarrow \nu_i + \bar{\nu}_i$	X	✓
$\gamma o u_i + \bar{ u}_i$	×	✓
$N + N \rightarrow N + N + \nu_i + \bar{\nu}_i$	X	
Absorption:		
$p + \bar{\nu}_e \rightarrow e^+ + n$	✓	✓
$n + \nu_e \rightarrow e^- + p$	×	✓
$ u_i + \bar{\nu}_i \rightarrow e^- + e^+ $	X	✓
$ u_i + \bar{\nu}_i \to \gamma $	X	✓
$N + N + \nu_i + \bar{\nu}_i \to N + N$	X	✓
Scattering:		
$\bar{\nu}_e + n \rightarrow \bar{\nu}_e + n$	✓	✓
$\{\nu_e, \nu_i\} + n \rightarrow \{\nu_e, \nu_i\} + n$	×	✓
$\{\nu_e, \bar{\nu}_e, \nu_i\} + p \to \{\nu_e, \bar{\nu}_e, \nu_i\} + p$	×	✓

with $v^{\alpha} = (0, u^{i}/W + \beta^{i}/\alpha)$, and $W \equiv -n_{\alpha}u^{\alpha} = \alpha u^{0}$ is the Lorentz-factor between normal and fluid observers. Note that by construction v^{α} is purely spatial, $n_{\alpha}v^{\alpha} = 0$.

2. Radiation evolution

Following Ref. [80], the dynamics of the radiation field can be expressed as

$$R^{\alpha\nu}_{\ :\nu} = -G^{\alpha},\tag{13}$$

where $G^{\alpha}=\int d\nu d\Omega (\kappa_{\nu}I_{\nu}-\eta_{\nu})N^{\alpha}$ is the radiation four-force density which describes the interaction between the radiation field and matter. In the energy-integrated moment formalism, the four-force terms can be written in the covariant form as

$$G^{\alpha} = \rho_0 [(\kappa^a E - \eta) u^{\alpha} + (\kappa^a + \kappa^s) F^{\alpha}], \tag{14}$$

where ρ_0 is the rest-mass density and η , κ^a , and κ^s represent the energy-averaged emissivity, absorption opacity, and scattering opacity, respectively. They are computed as functions of temperature, density, and the chemical potential via the major microphysical interactions listed in Sec. II D 2. Their analytic expressions, derived from Refs. [86,87], are bounded by the opposite limits of local thermal equilibrium (LTE) and free-streaming. In our implementation, we interpolate the limiting values following the method of interpolating $\mathcal{P}^{\alpha\beta}$ to accommodate

regions with different optical depths (see Appendix D for a detailed derivation). Note that, in LTE, η can be written by invoking Kirchhoff's law, using the frequency-integrated neutrino thermal equilibrium intensity \bar{B} : $\eta = \kappa^a 4\pi \bar{B} = \kappa^a a_R T^4$ [80,84], where T is the temperature of the fluid and a_R is a constant chosen based on the type of radiation. For photons, a_R is the radiation constant a, and for neutrinos, $a_R = 7aN_{\nu}/16$, where N_{ν} is the number of left-handed neutrino and right-handed antineutrino species contributing to thermal processes.

One can perform a normal projection of Eq. (13) and obtain the energy equation

$$\partial_t \bar{\tau} + \partial_i (\alpha^2 \sqrt{\gamma} R^{0i}) = \bar{s} - (\alpha^2 \sqrt{\gamma}) G^0, \tag{15}$$

where $\bar{\tau} = (\alpha^2 \sqrt{\gamma}) R^{00} = \sqrt{\gamma} \bar{E}$ is the radiation energy density and \bar{s} is given by

$$\bar{s} = \alpha \sqrt{\gamma} [(R^{00}\beta^{i}\beta^{j} + R^{0i}\beta^{j} + R^{ij})K_{ij}$$

$$-(R^{00}\beta^{i} + R^{0i})\partial_{i}\alpha]$$

$$= \sqrt{\gamma}(\alpha \bar{P}^{ij}K_{ij} - \bar{F}^{i}\partial_{i}\alpha).$$
(16)

Similarly, the spatial projection of Eq. (13) yields the momentum equations (see Refs. [80,84] for detailed derivations)

$$\partial_t \bar{S}_i + \partial_i (\alpha \sqrt{\gamma} R_j^i) = \alpha \sqrt{\gamma} \left(\frac{1}{2} R^{\alpha \beta} g_{\alpha \beta, i} - G_i \right),$$
 (17)

where \bar{S}_i is the radiation momentum density. They form the conserved variables of the dynamical equations. We note that, although described in different notations, Eqs. (15) and (17) are equivalent to the evolution equations in previous works (e.g., Eqs. (3.39) and (3.40) in Ref. [48] and Eqs. (16) and (17) in Ref. [50]) in conservative form.

We use the Harten-Lax-van Leer (HLL) approximate Riemann solver to evolve Eqs. (15)-(17), in which we adopt the characteristic speed of radiation field following Ref. [50] for the HLL fluxes at cell interfaces. Note that Eqs. (15)–(17) require the computation of $\mathcal{P}^{\alpha\beta}(E, F^{\alpha})$ and source terms G^{α} for closure. We adopt the prescription presented in Ref. [83] regarding the radiation pressure $\mathcal{P}^{\alpha\beta}(E,F^{\alpha})$, which is an interpolation of its optically thin and thick limits. Since the closure equation for $\mathcal{P}^{\alpha\beta}$ is a nonlinear function of E and F^{α} , the recovery of primitive variables requires a four-dimensional solver. A detailed description of the closure scheme and the recovery of the primitive variables are summarized in Appendices A and B, respectively. For the source terms, we adopted two versions: (i) the warm-up Simplified Scheme (Rad-Simp), which assumes a purely neutron-rich environment, where the net electron fraction Y_e is zero, and accounts for only the charged-current interaction of electron anti-neutrinos, and (ii) the Full Scheme (Rad-Full), which includes three

species of neutrinos: ν_e , $\bar{\nu}_e$, and ν_x , where ν_x is the sum of muon and tau neutrinos and their antiparticles, called the "heavy-lepton neutrinos" (Rad-Full). This scheme includes all the important interactions whose reaction rates are based on the evolved electron fraction Y_e using Eq. (18) and the temperature. A description of the source terms and the two schemes is summarized in Sec. II D 2 (see also Table I).

C. Evolution of metric and MHD fields

As in our previous magnetized NSNS studies, the Illinois GRMHD code solves the equations of ideal GRMHD in a conservative scheme via high-resolution shock capturing methods for the evolution of matter and magnetic field. The equations for metric, matter, and magnetic field, including radiation source terms, are given in Ref. [80]. Additionally, to compute Y_e used in the radiation source terms, we now evolve the quantity ρ_*Y_e following [48,50]

$$\partial_{t}(\rho_{*}Y_{e}) + \partial_{j}[(\rho_{*}Y_{e})v^{j}] = -\operatorname{sgn}(\nu_{i})\alpha\sqrt{\gamma}m_{N}\left(\frac{\eta - \kappa_{a}E}{\langle \epsilon_{\nu} \rangle}\right), \tag{18}$$

where

$$\operatorname{sgn}(\nu_i) = \begin{cases} 1 & \text{for } \nu_e, \\ -1 & \text{for } \bar{\nu}_e, \\ 0 & \text{for } \nu_x; \end{cases}$$

 m_N is the nucleon rest mass; $\langle \epsilon_{\nu} \rangle$ is the local mean energy of neutrinos, which is approximated as $F_5(\eta_{\nu})/F_4(\eta_{\nu})T$, with $F_k(\eta_{\nu})$ the Fermi integral $F_k(\eta_{\nu}) = \int_0^\infty x^k/(1+\exp(x-\eta_{\nu}))dx$, and $\eta_{\nu}=\mu_{\nu}/(k_BT)$, with μ_{ν} the chemical potential evaluated using the analytic expressions detailed in Appendix D 1. We note that the Fermi integrals can be efficiently evaluated using the polynomial approximations in Ref. [88].

We evolve the MHD equations using the standard HLL, approximate Riemann solver with a simpler, dissipative dispersion relation (see Eq. (50) in Ref. [89]). Required by the dispersion relation, the sound speed $c_s^2 = (dP/d\rho_0)_s/h$ consists of a cold and a thermal component of pressure (see Sec. II D), where h is the specific enthalpy and s is the specific entropy. The thermal part is based on an analytic expression for a semidegenerate neutron gas of non zero temperature. The analytic derivation and our implementation of the sound speed are described in detail in Appendix C 3. Notice that, as in standard hydrodynamic and MHD simulations, we integrate the ideal GRMHD equations on the whole numerical grid by imposing a tenuous atmosphere $\rho_{0,\text{atm}} = 10^{-10} \rho_{0,\text{max}}(0)$, constant-density where $ho_{0,\max}(0)$ is the initial maximum value of the rest mass of the system.

D. EOS, neutrino processes, and source terms

1. Finite-temperature treatment

Our NSNS binaries are modeled by a piecewise polytropic representation of the SLy nuclear EOS [59]. A cold EOS is adequate to model the NS prior to merger. However, during merger, considerable shock heating increases the internal energy. To account for this, we adopt an EOS that has both a thermal and cold contribution to the total energy density, $\mathcal{E} = \mathcal{E}_{\text{cold}} + \mathcal{E}_{\text{th}}$, and total pressure, $P = P_{\text{cold}} + P_{\text{th}}$. Specifically, $P_{\text{cold}} = \kappa_i \rho_0^{\Gamma_i}$, with κ_i and Γ_i the corresponding polytropic constant and the polytropic exponent in the restmass density range $\rho_{0,i-1} \leq \rho_0 \leq \rho_{0,i}$, respectively, fitted for SLy [90]. Note that the cold energy density is given by $\mathcal{E}_{\text{cold}} = P_{\text{cold}}/(\Gamma_i - 1)$. The thermal terms are the sum of nucleon and radiation (other than neutrino) contributions: (1) $\mathcal{E}_{\rm th} = \mathcal{E}_{\rm rad} + \mathcal{E}_{\rm nucl}$ and (2) $P_{\rm th} = P_{\rm rad} + P_{\rm nucl}$. The nucleon parts are based on a semidegenerate neutron gas expression that asymptotes to a Maxwell-Boltzmann gas in the nondegenerate limit. The radiation part includes photons and relativistic electron and positron pairs, which follow a Stefan-Boltzmann relation. Details of treatments of thermal EOS are summarized in Appendix C 1.

To implement the temperature-dependent thermal energy density and pressure in our simulations, we set our evolved value of \mathcal{E} to $\mathcal{E}_{cold}+\mathcal{E}_{th}$ using Eq. (C3) and solve for the temperature T. After obtaining T, we calculate the thermal pressure P_{th} base on Eq. (C4) and then obtain the total pressure $P = P_{th} + P_{cold}$ for the next iteration. This method provides a physically reasonable estimate of temperature. Note that such a formalism requires modifications in the MHD primitive solver for the computation of the Jacobian. The details of finding the temperature, as well as the modification of the primitives solver, are summarized in Appendix C2. See also Appendix D1 for a detailed description of this treatment of thermal energy density and pressure.

2. Opacity and emissivity

As shown in Eq. (14), the source terms G^{α} are determined by the radiation energy density E, energy flux F^{μ} , absorption opacity κ^{a} , scattering opacity κ^{s} , and emissivity η . The relevant interactions are summarized in Table I. For neutrino emission, they include the charged-current interactions

$$e^- + p \to n + \nu_e, \tag{19}$$

$$e^+ + n \to p + \bar{\nu}_e, \tag{20}$$

and three pair process interactions: electron-positron pair annihilation

$$e^{+} + e^{-} \rightarrow \nu_{i} + \bar{\nu}_{i};$$
 (21)

plasmon decay,

$$\gamma + \gamma \to \nu_i + \bar{\nu}_i;$$
 (22)

and nucleon-nucleon bremsstrahlung,

$$N + N \to N + N + \nu_i + \bar{\nu}_i. \tag{23}$$

Here, the subscript i represents all neutrino species, and N stands for nucleons. We can safely omit neutron decay $(n \to p + e^- + \bar{\nu}_e)$ from consideration here. The reason is that, even when the leptons in some regions become sufficiently hot to lift their degeneracy and partially remove the blocking factor that inhibits the decay at T=0, the decay time ($\gtrsim 14$ min) greatly exceeds the time it takes the HMNS remnant to collapse to a BH as well as the time for which we follow the evolution in our simulation.

The inverse reaction of the interactions above are responsible for neutrino absorption. Therefore, we need to compute both κ^a and η for Eqs. (19)–(23). Lastly, we also consider the neutral-current neutrino scattering off nucleons,

$$\nu_i + N \to \nu_i + N. \tag{24}$$

Note that we neglect electron-neutrino/antineutrino scattering for simplicity, noting that its contribution to the opacity is smaller than that for nucleon scattering by a typical factor of ~ 100 in the HMNS remnant (see also Ref. [91]). We do note for future work that electron scattering is inelastic and contributes to the thermalization of neutrinos [92,93], while nucleon scattering is conservative. We also note that for neutrino energies of ~ 10 MeV, cross sections of the charged-current absorptions of electron-type neutrinos are ~ 100 times greater than that of the electron-neutrino scattering [87].

Following Ref. [50], at every iteration, we first compute κ^a for the inverse of Eqs. (19) and (20) (charged-current interactions), κ^s for Eq. (24), and η for Eqs. (21) and (22) (thermal emission) based on the formalism in Ref. [86]. We then compute η for Eqs. (23) using Eq. (49) in Ref. [87]. These expressions require the knowledge of the fluid temperature and the chemical potential, which are computed analytically.

Next, using either κ_a or η computed above, we calculate η for the two charged-current interactions [Eqs. (19) and (20)] and κ_a for the three thermal pair processes. In the optically thick region, we impose the LTE condition and use the energy-integrated version of Kirchhoff's law,

$$\eta_{\rm Kir} = 4\pi \bar{B} \kappa^a, \quad \text{(charged current)},$$

$$\kappa^a = \eta/4\pi \bar{B}, \quad \text{(pair processes)}, \qquad (25)$$

where the energy-integrated equilibrium intensity $\bar{B}(T)$ is defined in Sec. II B 2. This method maintains the thermal equilibrium of neutrinos with the fluid in the optically thick

region. In the optically thin region, as the neutrinos can be out of thermal equilibrium, $\eta_{\rm Kir}$ may be inaccurate in estimating the emission of electron-type neutrinos. Therefore, we adopt an expression for the total emissivity by interpolating between $\eta_{\rm Kir}$ and $\eta_{\rm fs}$, where $\eta_{\rm fs}$ is the expression for the free-streaming emission rate for charged-current interaction in Ref. [86]. Here, we adopt an interpolation method similar to the M1 formalism [see Eq. (D2)], which estimates the emissivity based on optical thickness. Note that this is different from the interpolation methods in Ref. [50], which adopts a step function in terms of the optical depth.

III. NUMERICAL SETUP

A. Initial condition

We consider initial NSNS configurations in a quasiequilibrium circular orbit computed using our Compact Object Calculator (COCAL) code [94,95]. The binaries consist of two identical, irrotational NSs, modeled by the SLy nuclear EOS [59], as in Ref. [90]. Specifically, we use the SLyM2.7 (magnetized and unmagnetized, hereafter denoted as "Mag" and "Unmag," respectively) configurations treated previously in Ref. [96], for which the ADM mass of the system is $M_{\rm ADM} = M = 2.7 M_{\odot}$, and the companions have an initial coordinate separation of 45 km (see Table I in Ref. [96]). We define $M_0 = 3.02 M_{\odot}$ as the total rest mass of the system. We note that the SLy EOS satisfies current observational constraints on NSs. The maximum-mass configuration of an isolated star predicted by SLy is $M_{\rm sph}^{\rm max} = 2.06~M_{\odot}$ consistent with (i) $M_{\rm sph}^{\rm max} > 2.072^{+0.067}_{-0.066}~M_{\odot}$ from the NICER and XMM analysis of PSR J0740 + 6620 [97], (ii) $M_{\rm sph}^{\rm max} > 2.01_{-0.017}^{+0.017}~M_{\odot}$ from the NANOGrav analysis of PSR J1614-2230 [98], (iii) $M_{\rm sph}^{\rm max} > 2.01^{+0.14}_{-0.14}~M_{\odot}$ from the pulsar timing analysis of PSR J0348 + 0432 [99], and $M_{\rm sph}^{\rm max} > 2.14_{-0.18}^{+0.20}~M_{\odot}$ from the NANOGrav and the Green Bank Telescope [100]. In addition, SLy predicts that a star with a mass of 1.4 M_{\odot} has a radius of R=11.46 km and a tidal deformability of $\Lambda_{1.4} = 306.4$. These values are consistent with (i) $R = 11.94^{+0.76}_{-0.87}$ km obtained by a combined analysis of x-ray and GW measurements of PSR J0740 + 6620 [101], (ii) $R = 11.9^{+1.4}_{-1.4}$ km for a NS with mass in the range 1.16 M_{\odot} -1.6 M_{\odot} at the 90% credible level from the combined analysis of the LIGO/ Virgo Scientific Collaboration (LVSC) of the progenitors of GW170817 with the radio-timing observations of the pulsar J0348 + 0432 [99,102], and (iii) $\Lambda_{1.4} = 190^{+390}_{-120}$ for a NS with mass of 1.4 M_{\odot} at the 90% credible level from the LVSC analysis of GW170817 [102].

In the magnetized cases, the NSs are initially endowed with a dipolelike magnetic field generated by the vector potential [103]

$$A_{\phi} = \frac{\pi r_0^2 I_0 \varpi^2}{(r_0^2 + r^2)^{3/2}} \left[1 + \frac{15 r_0^2 (r_0^2 + \varpi^2)}{8 (r_0^2 + r^2)^2} \right], \qquad (26)$$

where r_0 and I_0 are the loop radius and current, which determine the geometry and strength of the magnetic field. $r^2 = \varpi^2 + z^2$, $\varpi_{\text{cm}}^2 = (x - x_{\text{cm}})^2 + (y - y_{\text{cm}})^2$, where $(x_{\rm cm}, y_{\rm cm}, 0)$ is the center of mass of the NS, determined by the coordinate of the maximum value of the rest-mass density. We set I_0 and r_0 such that the maximum value of the magnetic-to-gas-pressure ratio in the NS interior is $\beta_{\rm ratio}^{-1} \equiv P_{\rm mag}/P_{\rm gas} = 0.003125.$ The resulting initial magnetic field strength at the NS pole measured by a normal observer is $B_{\text{pole}} \simeq 10^{15.3}$ G. As in Ref. [32], we initially impose a low, variable atmospheric density $\rho_{0,\mathrm{atm}}$ that satisfies $\beta_{\text{ratio}}^{-1} = 100$ (see Eq. (4) in Ref. [32]). This setup mimics the magnetically dominant environment in a pulsarlike magnetosphere and validates the evolution of the exterior magnetic field. While the magnetic field we imposed is astrophysically large, we choose it so that following merger, the rms value of the field strength in the HMNS remnant is close to the values reported in very-highresolution (with a local resolution of $\Delta x = 17.5$ m) simulations [14], which showed that the KHI during merger can boost the rms B-field to 10^{15.5} G, with local values reaching 10¹⁷ G. Moreover, recent NSNS simulations [104] with a local numerical resolution of $\Delta x = 37$ m have also shown that a pure poloidal magnetic field with a strength of $\sim 10^{11}$ G in the interior of NSs can be amplified to rms values of $\sim 10^{16}$ G within the first ~ 5 ms after merger.

B. Neutrino insertion

To probe the effects of neutrino emission in our binary remnant, in all our cases, we insert the neutrino radiation at $t_{\rm insert} \sim 1350 M \approx 18$ ms (or $t-t_{\rm mer} \sim 226 M \sim 3$ ms after merger). The initial neutrino energy is based on the local fluid temperature, which is related by an analytic expression to the thermal energy density of fluid matter (see Sec. II D). In the low-density region where $\rho_0 = \rho_{\rm atm}$, we set $T = T_{\rm atm} = 10^3$ K, which is ~7 orders of magnitude lower than the temperature in the central region of HMNS and ~6 orders of magnitude lower than the treatment in Ref. [50].

In a hot NS in LTE, the energy density of each chirality state of ultrarelativistic neutrinos is

$$\mathcal{E}_{\nu,\text{state}} = \frac{7}{16} a T^4, \tag{27}$$

where a is the usual radiation constant. Let \mathcal{N}_{ν} be the number of neutrino species involved. Then, \mathcal{N}_{ν} has the maximum value of 6 when all the possible species of the Standard Model are considered (i.e., ν_e , $\bar{\nu}_e$, ν_μ , and their antiparticles). If we assume that only the left-handed

neutrino states couple to the weak interactions, then the energy density of each neutrino (and antineutrino) species i becomes

$$\mathcal{E}_{\nu,i} = \frac{7}{16} \mathcal{N}_{\nu} \, a \, T^4. \tag{28}$$

In Rad-Simp, we set $\mathcal{N}_{\nu}=1$ for $\bar{\nu}_{e}$, while in Rad-Full, we set $\mathcal{N}_{\nu}=1$ for both ν_{e} and $\bar{\nu}_{e}$ and $\mathcal{N}_{\nu}=4$ for ν_{x} . Note that the neutrino helicity may be flipped if the magnetic moment of the neutrinos is considered [105]. It is believed that the left-handed neutrino rotates to the right-handed one when the magnetic fields are transverse to neutrino propagation [106]. Other effects such as nonequilibrium quantum kinematics and coherent flavor evolution of neutrinos are also not captured in a thermal description [107]. Here, we ignore these effects.

At $t_{\rm insert}$, we assign the radiation primitive variables $E=\mathcal{E}_{\nu,i}$ for each species of neutrinos evolved and set the flux $F^{\alpha}=0$. This method can describe well the interior of the HMNS system where the density and temperatures are sufficiently high. In the outer regions of the merger remnant, matter may not have attained thermal equilibrium. However, as $\mathcal{E}_{\nu,i}$ scales as T^4 , its value in the atmosphere becomes negligibly small compared with the interior value. After setting the primitive variables, we compute the conserved variables $\bar{\tau}$ and \bar{S}_i and the source terms G^{α} for radiation evolution.

C. Neutrino evolution

After initializing E and F^{α} , we compute the conserved variables $(\bar{\tau}, \bar{S}_i)$ and reconstruct the primitive variables to the left and right of the grid cell surfaces using the monotonized central (MC) scheme [108]. Then, we compute the conserved quantities at the cell faces, together with the left- and right-going wave speed using the method described in Ref. [50] to obtain the flux quantities $\alpha^2 \sqrt{\gamma} R^{0i}$ and $\alpha\sqrt{\gamma}R_i^i$. Next, we compute the spatial derivative terms in Eqs. (15) and (17). After this, we compute the source terms \bar{s} in Eq. (15) and the term $R^{\alpha\beta}g_{\alpha\beta,i}$ in Eq. (17). With these values, we compute the opacities and emissivities using the method described in Appendix D, which depends on the matter density and temperature. To avoid overly stiff source terms, we set the maximum value of frequencyintegrated opacity at 10 km⁻¹, which could yield a sufficiently high optical depth ($\gtrsim 20$) to model the optically thick environment inside the high-density region. With this prescription, we can evolve the radiation field using explicit time stepping at a modest resolution. Finally, we compute the four-force terms which are required to evolve the radiation and MHD variables.

With the conserved quantities $(\bar{\tau}, \bar{S}^i)$ computed at a given time step, we now need to recover the primitive variables (E, F^i) . Because of the nonlinearity in the closure scheme,

a numerical root finder is needed. After the fluid velocity v^i is found by the MHD primitive solver, we adopt a 4D Newton-Raphson solver that computes the radiation primitive variables from the radiation evolution variables. The solver requires an 4×4 Jacobian matrix which governs the coefficient of the first-order terms. Line searches and backtracking methods are adopted for faster convergence [109]. The elements of the Jacobian can be evaluated analytically. Detailed descriptions, including the relevant equations, the expression for the Jacobian matrix, and other numerical settings are given in Appendix B.

D. Grid setup

In all our simulations, we use the same grid setup as in Ref. [96], which consists of two sets of nested boxes with nine refinement levels centered on each star, with adjacent levels differing in size and resolution by factors of 2. When two boxes overlap, they are replaced by a common box centered on the center of mass of the system. The half-length of each grid level is $(2835.26/2^{n-1})$ km, where n is the level number. The innermost refinement level has a grid spacing of $\sim 0.027 M \sim 111$ m. The number of grid points across the initial NS equatorial radius is $N_{\rm NS} = 82$. In all our cases, we use reflection (equatorial) symmetry over the orbital plane. As reported in Ref. [33], orbital plane symmetry does not impact the final outcome of the evolutions. The detailed grid hierarchy is summarized in Table II in Ref. [96].

E. Diagnostics

To verify the reliability of our numerical results, we monitored the L_2 normalized constraints computed from Eqs. (40) and (41) in Ref. [63]. In all our simulations, we find that during the inspiral the Hamiltonian constraint violation remains below 0.2% and oscillates between 0.2% and 0.4% during the HMNS phase. Then, it peaks at 0.8% at BH formation and then gradually approaches to \leq 0.1%. The normalized momentum constraint violation remains smaller than 0.4% during the inspiral and peaks at \sim 5.5% at BH formation and gradually relaxes to \sim 0.3% following the onset of the steady state. Similar values were reported in our long-term simulations of spinning NSNS modeled by piecewise EOSs [66].

After BH formation, we locate and track the position of the BH apparent horizon using the AHFinderDirect thorn [110]. The BH mass $M_{\rm BH}$ and its dimensionless spin parameter $\tilde{a}=a/M_{\rm BH}$ are calculated using the isolated horizon formalism [111]. We adopt a modified version of the PSIKADELIA thorn to compute the Weyl scalar Ψ_4 decomposed into s=-2 spin-weighted spherical harmonics at different radii between $50M\sim200~{\rm km}$ and $300M=1200~{\rm km}$ [112]. We compute the rest-mass accretion rate \dot{M} following Eq. (A11) in Ref. [113]. The mass of escaping matter (ejecta) is computed as

 $M_{\rm esc}=-\int_{r>r_0}\sqrt{\gamma}\rho_0n_\mu u^\mu d^3x$, where the integral is restricted by the two conditions: (i) $-1-u_0>0$, where u^0 is the time component of 4-velocity, and (ii) having positive radial velocity $v^r>0$. $M_{\rm esc}$ is computed at various coordinate radii r_0 from $30M\sim 120$ km to $100M\sim 400$ km in order to verify that it is r_0 independent. We compute the rate of escaping mass $\dot{M}_{\rm esc}=-\int v^r\sqrt{\gamma}\rho_0n_\mu u^\mu d\mathcal{S}$ [113] flowing across spherical surfaces at coordinate radii between $r_{\rm ext}=50M\sim 200$ km and $350M\sim 1400$ km.

To track the conservation and transport of angular momentum, we compute the angular momentum carried off by gravitational radiation $J_{\rm GW}$ using Eqs. (3.22)–(3.24) in Ref. [112]. We also compute the angular momentum carried off by fluid, EM field, and neutrinos via

$$J_{i,\text{fluid}} = \int_{V} \epsilon_{ijk} x^{j} T_{\text{fluid}}^{kl} dV, \qquad (29)$$

$$J_{i,\text{EM}} = \int_{\mathcal{V}} \epsilon_{ijk} x^{j} T_{\text{EM}}^{kl} d\mathcal{V}, \tag{30}$$

$$J_{i,\nu} = \int_{V} \epsilon_{ijk} x^{j} R^{kl} d\mathcal{V}. \tag{31}$$

Here, ϵ_{ijk} is the three-dimensional (3D) Levi-Civita symbol, and $T_{\rm fluid}^{\alpha\beta}$ and $T_{\rm EM}^{\alpha\beta}$ are the stress-energy tensors associated with the perfect fluid and the electromagnetic field given by Eqs. (44) and (42) in Ref. [80], respectively. We monitor the conservation of the total mass and angular momentum $M_{\rm int}$ and $J_{\rm int}$ computed via Eqs. (19)-(22) in Ref. [114], which coincide with the ADM mass and ADM angular momentum initially. In all our evolved configurations, we find that the total mass and total angular momentum are conserved to within $\sim 1\%$ and $\sim 5\%$, respectively. In addition, we monitor the conservation of the rest mass $M_0 = \int \rho_* d^3x$, where $\rho_* \equiv -\sqrt{\gamma}\rho_0 n_\mu u^\mu$, which is conserved to within ~0.6%. Moreover, we compute the outgoing EM Poynting and neutrino luminosities $L_{\rm EM} = -\int T_0^{r({\rm EM})} \sqrt{-g} d\mathcal{S}$ and $L_{\nu} = -\int R_0^r \sqrt{-g} dS$, across spherical surfaces of coordinate radii between $r_{\rm ext} = 50M \sim 200 \text{ km}$ $350M \sim 1400$ km. For Mag + Rad-Full cases, we compute the neutrino luminosity for each species. To study the effect of neutrinos on MRI in our evolution, we compute the number of grid points resolved by the fastest growing MRI mode λ_{MRI} [64], namely, the λ_{MRI} -quality factor $Q_{\rm MRI} \equiv \lambda_{\rm MRI}/dx$, where dx is the local grid spacing. A successful capture of MRI must satisfy the condition $Q_{\mathrm{MRI}} \gtrsim 10$, and λ_{MRI} must fit inside the remnant [115,116]. Lastly, to study the effective turbulent viscosity due to the magnetic field and compare it to the effective viscosity induced by neutrinos [see Eq. (E1)], we compute the effective Shakura-Sunyaev α_{SS} parameter [117] by

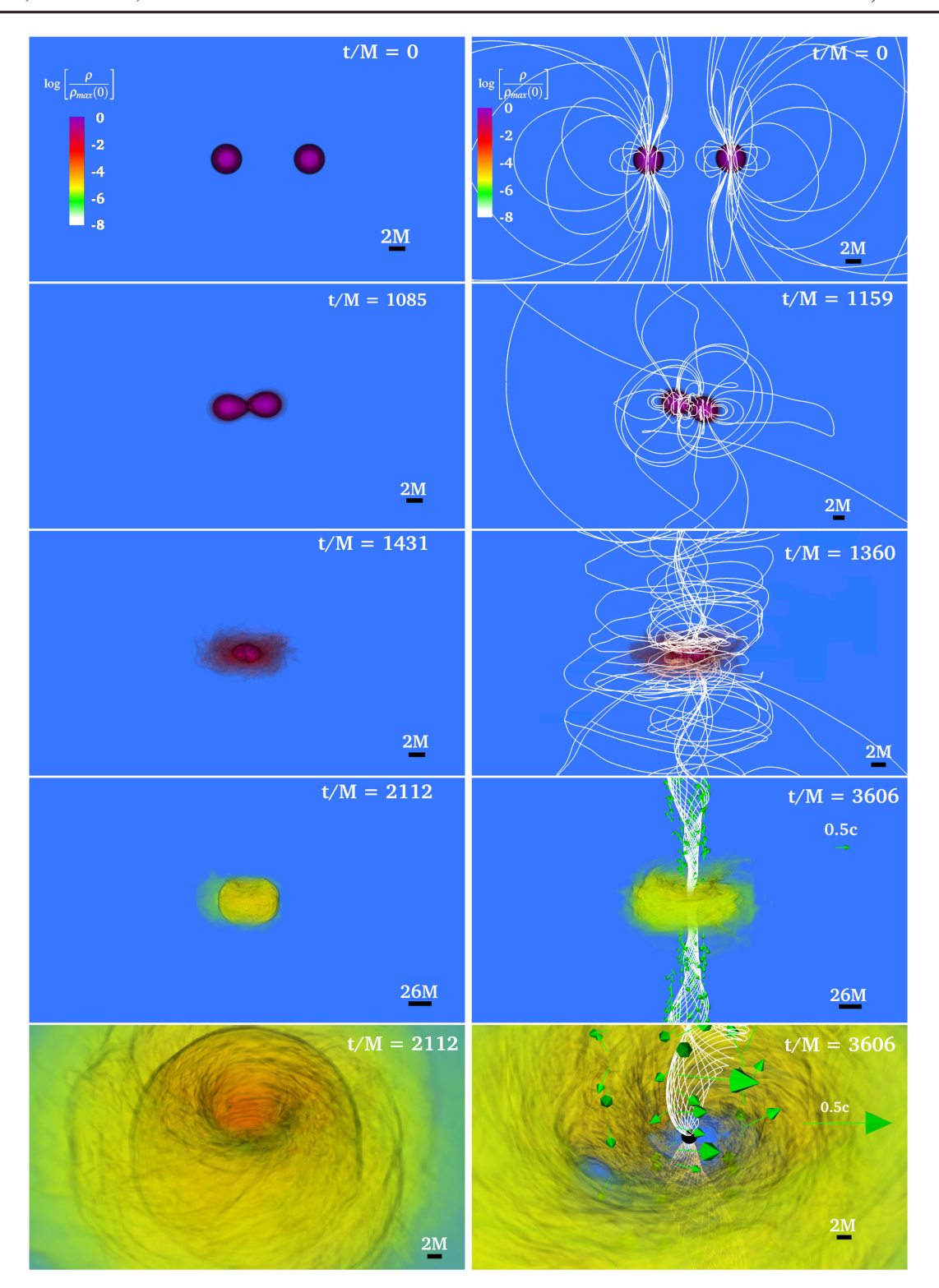


FIG. 1. Three-dimensional volume rendering of the rest-mass density ρ_0 , normalized to its initial maximum value $\rho_{0,\text{max}} = 8.65 \times 10^{14} \text{ g cm}^{-3}$ (log scale), at selected times for Unmag (left) and Mag (right) cases (see Table II). The bottom right panel highlights the system after an incipient jet is launched. White lines shows the magnetic field lines emanating from the BH polar region, and the arrows indicate plasma velocities. The BH apparent horizon is shown as a black sphere. Here, $M = 2.7 \ M_{\odot} = 0.0133 \ \text{ms} = 3.99 \ \text{km}$ is the ADM mass.

 $\alpha_{\rm SS} \equiv \langle T_{\hat{r}\hat{\phi}}^{\rm EM}/\langle P \rangle \rangle_{_{I}}$ (see Eq. (26) in Ref. [118]), where the brackets denote a time-averaged quantity.

IV. EVOLUTION RESULTS

A. General properties of merger

The inspiral phase of the NSNS models listed in Table II is summarized in the first rows of Fig. 1. The frozen-in magnetic field is simply advected with the matter, while GWs carry away angular momentum, causing the orbital separation to shrink. We observe that all our cases merge roughly at $t_{\rm merge} \sim 15$ ms (see the second row and Table III in Ref. [96]). Here, we define the merger time $t_{\rm merge}$ as the time of peak GW amplitude. Following merger, a transient remnant forms with two, massive central cores rotating about each other that gradually coalesce. They form a highly differentially rotating HMNS, surrounded by a low-density cloud of matter from fall-back tidal debris.

As weare primarily concerned with the influence of neutrino emission on the launching of jets, we inserted neutrinos in Unmag and Mag at $t-t_{\rm merge}\approx 226\sim 3$ ms following merger (see first row in Fig. 2). In the following sections, we describe the final outcome of our simulations with different magnetic field content, neutrino transport, and the two microphysics versions. For comparison, we also include the SLy cases without neutrinos previously treated in Ref. [96].

As mentioned before, we denote the unmagnetized case as "Unmag" and its simplified neutrino radiation counterpart as "Unmag + Rad-Simp". The magnetized case is denoted as "Mag," and its neutrino radiation counterparts is denoted as "Mag + Rad-Simp" and "Mag + Rad-Full," based on their microphysical schemes (see Table I). Important quantities from these simulations are summarized in Table II.

B. Final configuration

1. Unmagnetized NSNS binaries

The left column in Fig. 1 displays several key moments during the evolution of Unmag, while its neutrino counterpart is shown in the left column in Fig. 2. The HMNS remnant in Unmag lasts for approximately $t - t_{\text{merge}} =$ $700M \approx 9.3$ ms (see the left column of Fig. 1), followed by the formation of a highly spinning BH with a mass $M_{\rm BH} \simeq$ $2.55~M_{\odot}$ and spin $a_{\rm BH}/M_{\rm BH} \simeq 0.70$ immersed in an accretion disk of radius $\sim 25M \approx 100$ km which contains \sim 2.2% of the total mass of the system (see Table II). By contrast, the HMNS remnant in Unmag + Rad-Simp collapses at $550M \approx 7.4$ ms forming a spinning BH with mass $M_{\rm BH} = 2.59~M_{\odot}$ and spin parameter $a_{\rm BH}/M_{\rm BH} = 0.71$ immersed in an accretion disk that extends to $\sim 40M \approx$ 160 km and contains ~1.8% of the total rest-mass of the binary (see the left column of Fig. 2). We observe that neutrino radiation induces an effective viscosity (see

Key simulation parameters. Here, $au_{HMNS}[ms]$ is the lifetime of the HMNS, and $t_{BH}[ms]$ is the BH formation time. The mass and the dimensionless spin parameter of the BH remnant are given by $M_{
m BH}[M_\odot]$ and $ilde{a}=a_{
m BH}/M_{
m BH}$, respectively. $\Delta ar{E}_{
m GW}\equiv E_{
m GW}/M_{
m ADM}$ and $\Delta ar{J}_{
m GW}\equiv J_{
m GW}/J_{
m ADM}$ denote the fraction of energy and angular momentum carried HMNS pole just before collapse. $L_{\rm EM}[{\rm erg\,s^{-1}}]$ is the Poynting luminosity driven by the jet, which is averaged over the last \sim 5 ms before the termination of our simulations. $\alpha_{\rm SS}$ espectively. $L_{\nu}(\text{erg s}^{-1})$ is the total neutrino luminosity, and $\Delta \bar{J}_{\nu}$ he effective Shakura-Sunyaev magnetic viscosity parameter. gravitational 'not applicable off by

Model	$\tau_{\rm HMNS}$	$t_{ m BH}$ M	$_{ m BH}$ $ ilde{a}$	$ au_{ m HMNS}$ $t_{ m BH}$ $M_{ m BH}$ $ ilde{a}$ $\Delta ar{E}_{ m GW} imes 10^{-2}$	$\Delta J_{\rm GW} \times 10^{-1}$	M M	$\Delta J_{ m GW} imes 10^{-1} \ \dot{M} \ M_{ m disk}/M_0^{(\dagger)} imes 10^{-2a} \ M_{ m esc}/M_0 imes 10^{-2} \ B_{ m rms} \ L_{ m EM}$	$M_{\rm esc}/M_0 \times 10^{-2}$	$B_{ m rms}$ $L_{ m EM}$ $lpha_{ m SS}$	$L_{ m knova}$ $ au_{ m peak}$ $L_{ u}$ $\Delta J_{ u} imes 10^{-4}$	$\Lambda \bar{J}_{\nu} \times 10^{-4}$
Unmag ^b	8.43	8.43 23.1 2.55 0.70	55 0.7	0 3.23	3.31	4.07	2.24	0.13		10 ^{41.5} 0.5	
$Unmag + Rad\text{-}Simp 7.55 22.0 \ \ 2.59 \ \ 0.71$	7.55	22.0 2.	59 0.7	71 3.09	3.24	4.00	1.89	0.11		$10^{41.1} \ 0.14 \ 10^{52.0}$	0.7
Mag ^b	9.36	9.36 24.5 2.45 0.62	45 0.6	52 2.63	2.95	2.91	6.16	0.89	10 ^{16.3} 10 ^{52.8} 0.02–0.07 10 ^{41.5} 0.47	.07 10 ^{41.5} 0.47	
Mag + Rad-Simp	4.11	19.2 2.55 0.69	55 0.6	2.40	2.75	1.81	3.33	0.58	$10^{16.1} \ 10^{52.9} \ 0.01-0$	$10^{16.1} \ 10^{52.9} \ 0.01-0.08 \ 10^{41.5} \ 0.41 \ 10^{52.6}$	5.5
Mag + Rad-Full	5.24	5.24 20.7 2.51 0.68	51 0.6	1.55	2.88	2.15	4.58	0.95	$10^{16.0} \ 10^{52.8} \ 0.02-0$	$10^{16.0} \ 10^{52.8} \ 0.02-0.09 \ 10^{41.6} \ 0.46 \ 10^{53.1}$	44.0

 $^{a}M_{0}$ denotes the initial total rest mass of the system. b Cases we treated previously in Ref. [96].

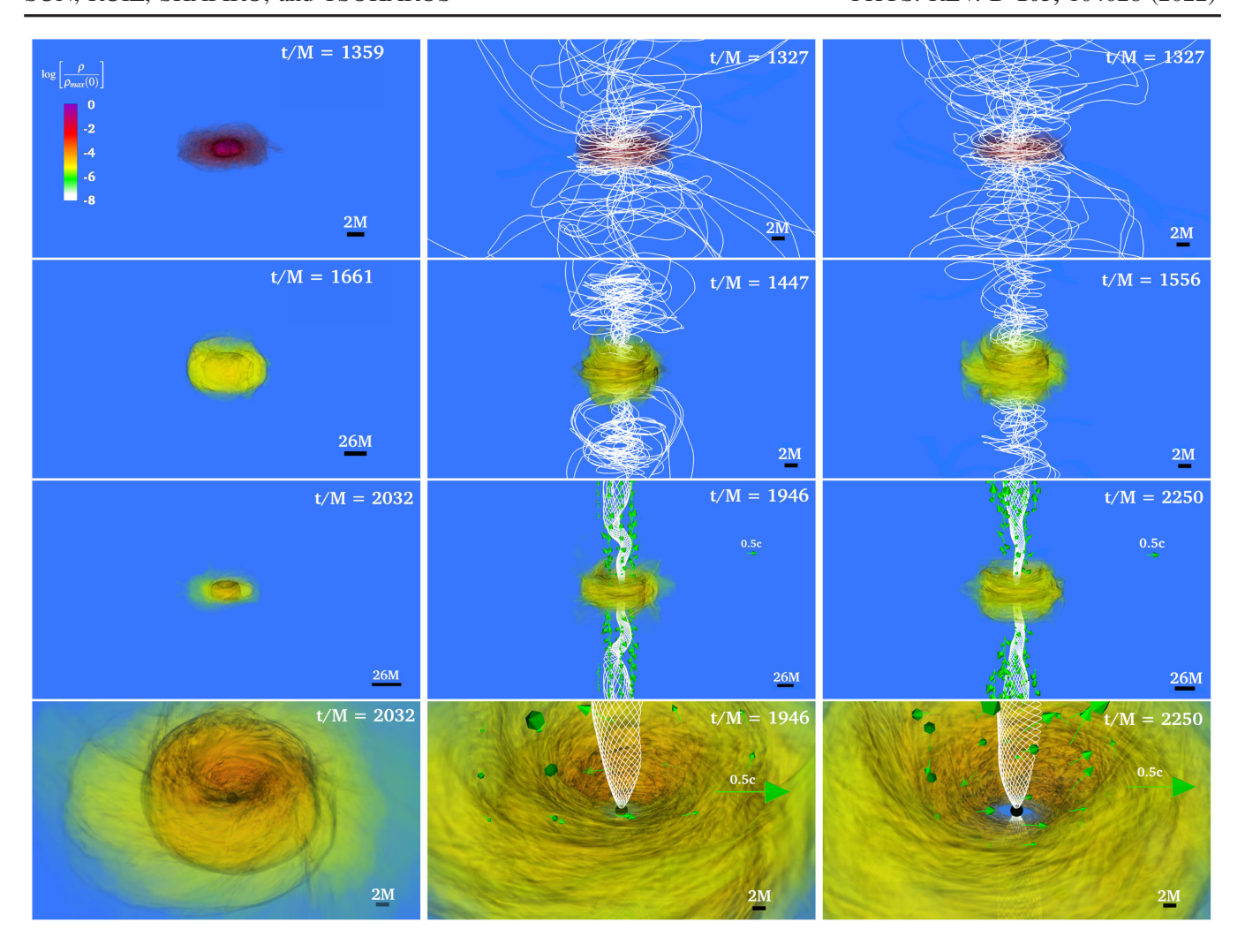


FIG. 2. Three-dimensional volume rendering of the rest-mass density ρ_0 , normalized to its initial maximum value $\rho_{0,max} = 8.65 \times 10^{14} \text{ g cm}^{-3}$ (log scale), at selected times for Unmag + Rad-Simp (left), Mag + Rad-Simp (middle), and Mag + Rad-Full (right) cases (see Table II). The bottom middle and right panels highlight the system after an incipient jet is launched. White lines shows the magnetic field lines emanating from the BH polar region, and the arrows indicate plasma velocities. The BH apparent horizon is shown as a black sphere. Here, $M = 2.7~M_{\odot} = 0.0133~\text{ms} = 3.99~\text{km}$ is the ADM mass.

below), causing the angular velocity of the Unmag + Rad-Simp transient to become almost uniform in the inner core. This causes an earlier collapse compared with Unmag. In both cases, the accretion rate M begins to settle after $t - t_{\rm BH} \sim 380 M \simeq 5$ ms, reaching a value of $\sim 4 M_{\odot} \text{s}^{-1}$ (see Fig. 3). The insert displays the fraction of the dynamical ejection of rest mass following merger. We find that neutrinos do not significant enhance the ejection of matter. In both cases, $M_{\rm esc}/M_0 \simeq 1 \times 10^{-3}$. These values are consistent with those reported previously in Refs. [119,120]. We note that transient kilonova signatures powered by the radioactive decay of heavy elements formed via rapid neutron capture (r-process) nucleosynthesis can be detected if the ejected mass is greater than $10^{-3} M_{\odot}$ [121,122]. We compute the estimated peak bolometric luminosity and the rise time of kilonova for these cases using an analytical model recently derived in Ref. [41], which assumes that $M_{\rm esc}$ is spherically distributed and expanding homologously (see Eqs. (8)–(10) in Ref. [96]). We find that the peak kilonova luminosities of the two unmagnetized cases are $L_{\rm knova} \approx 10^{41.3\pm0.2}$ erg s⁻¹, the rise time is ~4–11h, and an effective temperature $T_{\rm peak} \sim 10^{3.4}$ K (see Table II). Converting the peak temperature to peak wavelength using the relation $\lambda_{\rm peak} = 1.35 \times 10^3$ nm($T_{\rm peak}/10^{3.33}$ K)⁻¹ [41], we find $\lambda_{\rm peak} \sim 1150$ nm. This emission may be observed by current or future instruments such as ALMA or the Vera C. Rubin observatory [123,124].

2. Magnetized NSNS binaries

The basic dynamics and final outcome of the magnetized cases in Table II are displayed in the right column of Fig. 1 and in the middle and right columns of Fig. 2 for case Mag,

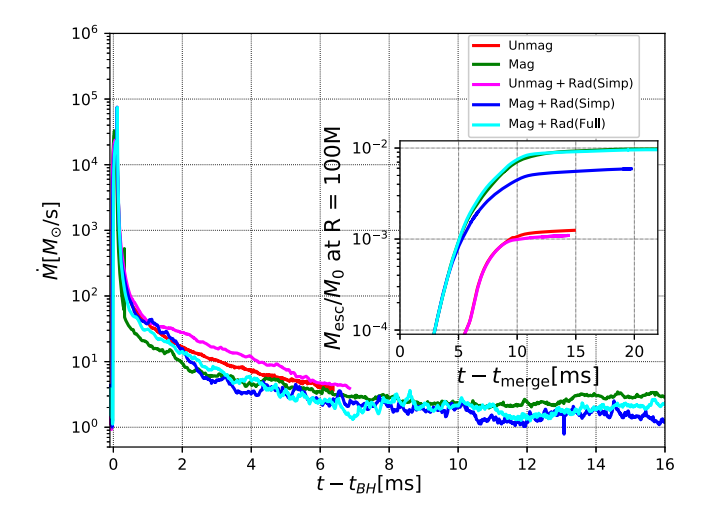


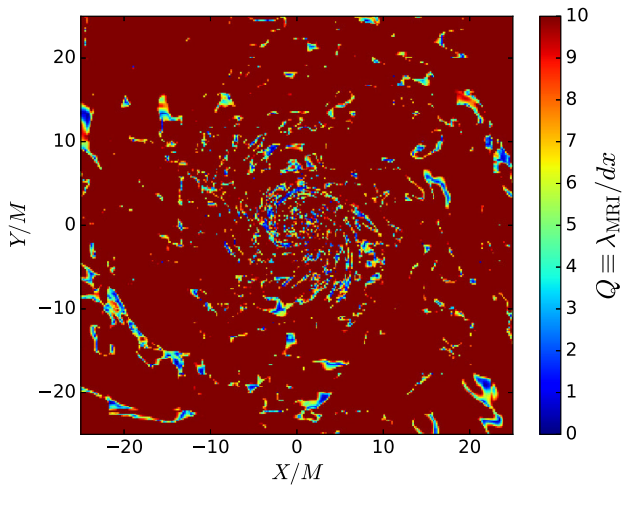
FIG. 3. Rest-mass accretion rate as a function of time for all cases in Table II. The insertion displays the ejected rest-mass fraction $M_{\rm esc}/M_0$ measured on a coordinate sphere of radius $r=100~{\rm M}\approx 400~{\rm km}$ following merger.

Mag + Rad-Simp, and Mag + Rad-Full, respectively. Consistent with our previous results (see e.g., [26,96]), in all cases we find that a magnetically supported jet is launched following the collapse of the transient HMNS. These results may indicate that incipient jets are the typical outcome of NSNS undergoing delayed collapse.

Figure 4 shows that during the HMNS phase the wavelength λ_{MRI} of the fastest-growing mode is resolved by more than ten grid points (top panel). In addition, λ_{MRI} fits in the bulk of the HMNS (bottom panel), i.e., the region where the rest-mass density is $\rho_0 \gtrsim 10^{11} \text{ g/cm}^3$, well above of the floor density. Therefore, we conclude that MRI-induced turbulence is resolved and operating in our systems. We observe that angular momentum is transferred from the inner to the outer layers of the HMNS due both to magnetic winding and magnetic turbulence. Magnetic winding operates on a timescale of [125,126]

$$\begin{split} \tau_{\rm A} &\sim \frac{R_{\rm HMNS}}{v_{\rm A}} \\ &\sim 1 \ {\rm ms} \left(\frac{\rho}{10^{15} \ {\rm g/cm^3}} \right)^{1/2} \left(\frac{|B|}{10^{15} \ {\rm G}} \right)^{-1} \left(\frac{R_{\rm HMNS}}{10^5 \ {\rm cm}} \right). \ (32) \end{split}$$

The transport of angular momentum induces the formation of a massive, nearly uniformly rotating core surrounded by a Keplerian cloud of matter (see Fig. 5). Here, $v_{\rm A} \sim |B|/\sqrt{4\pi\rho}$ is the Alfvén speed, B is the strength of the magnetic field, and ρ and $R_{\rm HMNS}$ are the characteristic restmass density and radius of the remnant, respectively. Similar results are reported in Ref. [96] and, together with the discussion of neutrino viscosity below, suggest that neutrino effects do not influence the growth of MRI. We note that the relativistic smoothed particle hydrodynamics



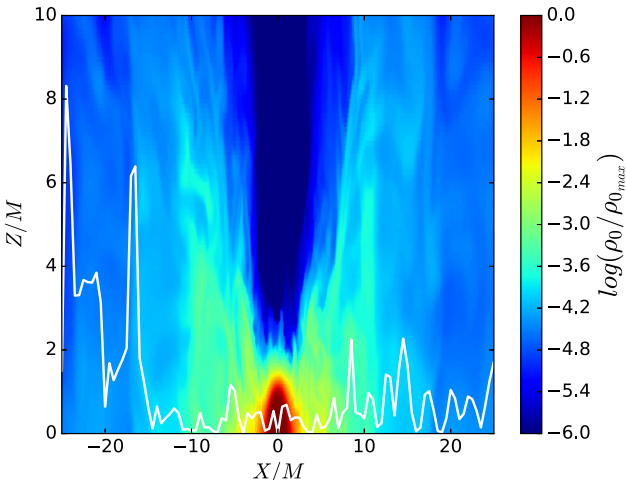


FIG. 4. Contours of the quality factor $Q = \lambda_{\text{MRI}}/dx$ on the equatorial plane (top) and the rest-mass density of the transient HMNS normalized to its initial maximum value (log scale) along with λ_{MRI} (white line) on the meridional plane (bottom) for Mag + Rad-Full at $t - t_{\text{GW}} \approx 390 M \sim 5.2$ ms. Similar behavior is observed in all magnetized cases in Table II (see Fig. 7 in Ref. [96]).

simulations in Ref. [127] suggest that the growth rate of the MRI is significantly reduced by neutrino effects if the magnetic field is lower than $\lesssim 10^{14}$ G inside the HMNS. However, it is expected that typical vales of the magnetic field in the HMNS are $\gtrsim 10^{15.5}$ G due to the KHI [15,128].

Calculating the effective Shakura-Sunyaev α_{SS} parameter in the HMNS for the magnetized cases in Table II, we found that it ranges between 0.01 and 0.09. Similar values have been reported in high-resolution NSNS merger simulations (see, e.g., Ref. [130]). These results explain why turbulent magnetic fields can redistribute angular momentum and damp the differential rotation effectively on an effective turbulent magnetic viscous timescale due to MRI (see Eq. (7) in Ref. [126]),

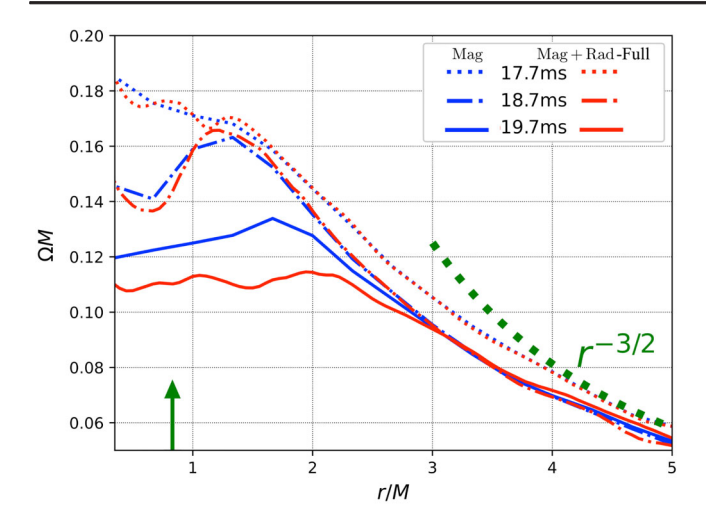


FIG. 5. Average rotation profile of the HMNS (see Eq. 2 in Ref. [129]) for Mag (blue) and Mag + Rad-Full (red) on the equatorial plane following merger along with the Keplerian angular velocity profile. Times after neutrino insertion are included. The arrow marks the coordinate radius containing 50% of the rest mass of the HMNS.

$$\begin{split} \tau_{\rm vis} &\sim (\alpha_{\rm SS}\Omega)^{-1} \sim R_{\rm HMNS}^{3/2} M_{\rm HMNS}^{-1/2} \alpha_{\rm SS}^{-1} \\ &\sim 1 \ {\rm ms} \left(\frac{\mathcal{C}}{0.3}\right)^{-3/2} \left(\frac{M_{\rm HMNS}}{3 \ M_{\odot}}\right) \left(\frac{\alpha_{\rm ss}}{10^{-2}}\right)^{-1}, \quad (33 \ \end{split}$$

where $M_{\rm HMNS}$ is the characteristic mass of the HMNS and $\mathcal{C} = M_{\rm HMNS}/R_{\rm HMNS}$ is its compaction.

As described in Ref. [127], the diffusion of neutrinos trapped in the HMNS also induces an angular momentum transport. We observe (see Fig. 5) that neutrino transport helps drive the central core of the HMNS to nearly uniformly rotation, causing the HMNS in the Mag + Rad cases to collapse ~4 ms faster than in Mag (see Table II). Because of this effect, more material from the external layer of the HMNS remains inside the innermost stable circular orbit (ISCO) during the BH formation, which induces the formation of lighter accretion disks ($\lesssim 25\%$) in the Mag + Rad cases than in the Mag case (see Table II). Note that neutrino radiation can also help trigger the collapse of the HMNS by reducing the thermal support, though we do not observe a significant change in the gas temperature in our simulations. We caution that the collapse time of a short-lived HMNS depends on the strength of the seed magnetic field (see, e.g., Fig. 2 in Ref. [22]), as well as on the numerical resolution, even in nonmagnetized evolutions [131,132].

As described in Refs. [44,127], for MRI wavelengths shorter than the neutrino mean free path, neutrino radiation induces a drag on the velocity with a damping rate independent of the wavelength. Here, we study the viscosity and dragging effect due to neutrinos on the suppression of MRI. Comparing the analytical estimates of the effective viscosity due to neutrino diffusion ν_{neutrino} [see Eq. (E1)] and the effective viscosity induced by MHD

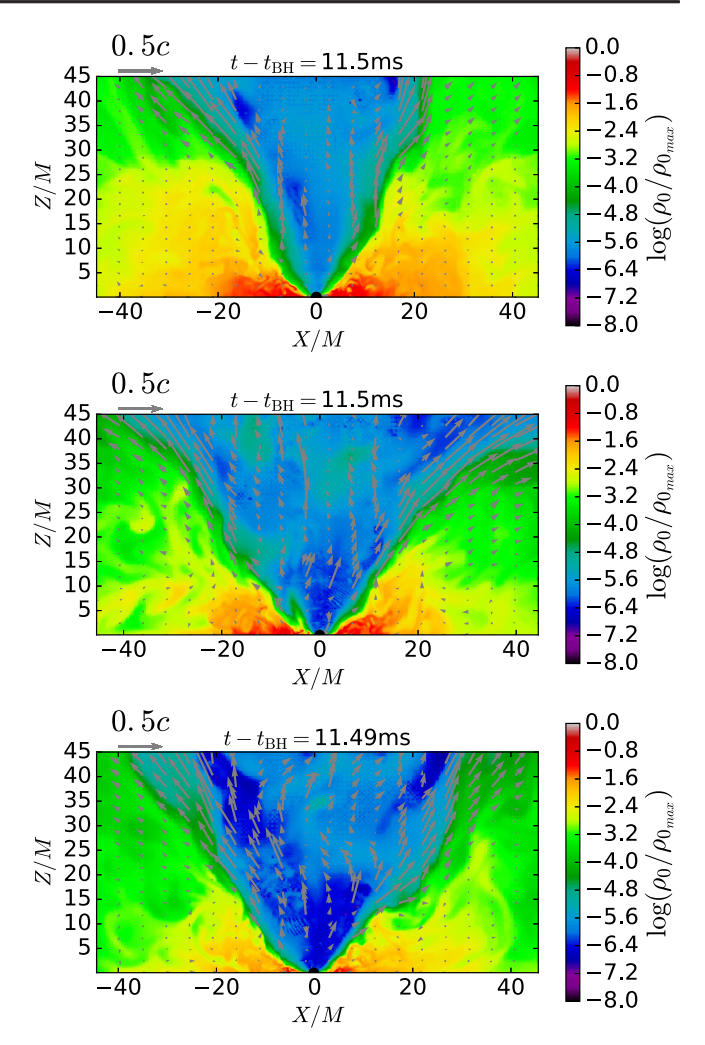


FIG. 6. Rest-mass density normalized to its initial maximum value $\rho_{0,\text{max}}$ (log scale) on the meridional x-z plane for Mag (top), Mag + Rad-Simp (middle), and Mag + Rad-Full (bottom) cases at $t-t_{\text{BH}} \approx 11.5$ ms. A BH apparent horizon is displayed as a black semicircle, while arrows indicate fluid velocities.

turbulence using an α -disk model ν_{MHD} [133,134], we find that ν_{neutrino} does not have an significant effect on the suppression of MRI both inside HMNS and in the disk. The magnetic field strength in the HMNS in all our simulations exceeds the critical strength of the magnetic field, $B_{\rm crit} \sim 10^{14}$ G, below which the viscosity can significantly suppresses the growth of the MRI [127]. The viscous effect is controlled by the Elsasser number $E_{\nu} \equiv v_A^2/(\nu_{\rm neutrino}\Omega)$ [44,135,136], which is $E_{\nu} \gtrsim 10$ in our simulations. This value indicates that the effective viscosity induced by neutrinos has little effect on to the growth of MRI (see Figs. 4 and 7 in Ref. [96]). On the other hand, when the wavelength of the fastest-growing MRI mode is shorter than the mean free path of heavy-lepton neutrinos (which gives the most restrictive constraint among all species), neutrinos can induce a drag force. Using the scaling relation of the heavy lepton neutrino mean free path [44]

$$l_{\nu} = 10^4 \left(\frac{\rho_0}{10^{13} \text{ g cm}^{-3}}\right)^{-1} \left(\frac{T}{10 \text{ MeV}}\right)^{-2} \text{ cm},$$
 (34)

we observe that neutrino drag becomes significant only when the magnetic field is lower than the critical magnetic field strength ($\lesssim 10^{14}$ G) in the HMNS, and hence neither the effective neutrino viscosity nor drag force has a distinguishable influence on the development of MRI in our simulations during the HMNS phase.

We also estimate analytically the shear viscosity due to nucleon-nucleon scattering using Eq. (14) in Ref. [137] as a function of T and ρ_0 . We note that this expression assumes nonsuperfluid matter and ignores the collisions of electrons and muons. We find that it has a comparable magnitude as $\nu_{\rm neutrino}$ deep inside the HMNS but decreases quickly as r > 5 km (see Fig. 13 in Appendix E). Therefore, we conclude that MHD-induced viscosity is the dominant viscosity source. The transport of angular momentum in the neutrino-involved cases is more substantial due to both MRI and neutrino-induced effective shear viscosity (see Appendix E for more detailed discussions regarding viscosities). Note that we ignore the bulk viscosity due to Urca interactions and hyperons processes, since the shear viscosity is most important in transporting and redistributing angular momentum in the HMNS, which leads to its collapse. Bulk viscosity is mainly important during the late inspiral phase [138].

The transient HMNS remnant collapses to a BH with mass $M_{\rm BH} \sim 2.4 - 2.6~M_{\odot}$ and with spin $a/M_{\rm BH} \sim 0.62$ for Mag and $a/M_{\rm BH} \sim 0.68$ for Mag + Rad cases (see Table II). By $t - t_{\rm BH} \sim 450 M \sim 6$ ms following BH formation, when the accretion rate M begins to settle down (see Fig. 3), we observe that magnetic-dominated regions $(B^2/(8\pi\rho_0) \gtrsim 1)$ above the BH poles begin to expand and reverse the fall-back debris inflow. Magnetic winding above that BH poles, which began during the HMNS phase (see the third-row right panel in Fig. 1 and top panels in Fig 2), induces the formation of a tightly wound helical magnetic funnel. As the accretion near the equator proceeds and neutrino processes take place, the baryon-loaded environment inside the funnel gradually becomes thinner, allowing a magnetically driven jet to emerge eventually (see bottom panels in Figs. 1 and 2). We note that in the Mag + Rad cases a magnetically supported jet is launched after $t - t_{\rm BH} \sim 750 M \sim 10$ ms, while in Mag, it is launched at $t - t_{\rm BH} \sim t - t_{\rm BH} \sim 1800 M \sim 24$ ms [96]. Figure 6 displays the rest-mass density on the meridional plane for the above cases. We observe that the rest-mass density inside the funnel of the Mag + Rad cases is a factor of ~ 10 lighter than in Mag. This suggests that neutrino radiation reduces the baryon-loaded environment in the polar region above the BH poles. As we do not observe an enhancement of the magnetic field strength following BH formation, the funnel emptying due to neutrinos makes it easier for the magnetic pressure gradients above the BH poles to overcome the fallback ram pressure of the infalling material. Similar results have also been reported in Ref. [56]. We note that by $t-t_{\rm BH}\sim 6$ ms the accretion rate is $\sim 2~M_{\odot}/{\rm s}$ and the rest mass of the accretion disk is $\sim 0.2~M_{\odot}$ (see Table II). Therefore, the disk will be accreted in $\Delta t \sim M_{\rm disk}/\dot{M} \sim 0.1$ s, roughly consistent with the lifetime of a sGRB central engine [139,140].

Figure 7 displays the outgoing Poynting luminosity $L_{\rm EM}$ as a function of $t-t_{\rm jet}$ for cases in Table II. We observe that $L_{\rm EM}\sim 10^{53}~{\rm erg\,s^{-1}}$. As pointed out in Ref. [96], the Poynting luminosity roughly agrees with the theoretical range we derived in Ref. [141] for BH + disk + jet systems arising from compact binary mergers containing NSs or from the magnetorotational collapse of massive stars. The luminosities are also in accord with the narrow range characterizing the observed luminosity distributions of over 400 GRBs [60,142].

Following Ref. [96], we assess if the BZ mechanism is likely operating in the BH + disk remnant. We begin by comparing the outgoing Poynting luminosity $L_{\rm EM}$ in our simulations (see Fig. 7) with that from the BZ mechanism [143]

$$L_{\rm BZ} \sim 10^{52} \left(\frac{\tilde{a}}{0.75}\right)^2 \left(\frac{M_{\rm BH}}{2.8 \ M_{\odot}}\right)^2 |B_{\rm p}|_{16}^2 \ {\rm erg \ s^{-1}}, \quad (35)$$

where $|B_p|_{16} \equiv |B_p|/10^{16}$ G is the strength of the magnetic field at the BH poles. The EM Poynting luminosity in our simulation is $\sim 10^{53}$ erg s⁻¹ (see Table II). Next, we estimate that $|B_p| \sim 10^{16}$ G, and hence $L_{\rm BZ} \sim 10^{52}$ erg s⁻¹, in rough agreement. We also estimate the magnetic field-to-BH angular frequency ratio Ω_F/Ω_H on a meridional plane passing through the BH centroid and along coordinate semicircles of radii $r_{\rm BH}$ and $2r_{\rm BH}$. We find that in all cases

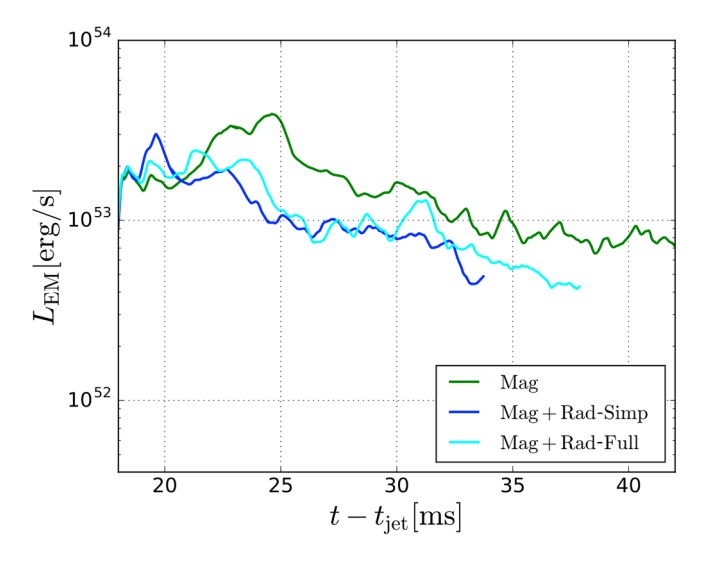


FIG. 7. Outgoing EM Poynting luminosities extracted at a coordinate sphere of radius $r = 160M \sim 640$ km as a function of $t - t_{\rm jet}$ for all magnetized cases in Table II.

 $\Omega_F/\Omega_H \sim 0.2$ –0.6. As pointed out in Ref. [96], deviation from the split-monopole value ~ 0.5 [144] may be due to artifacts such as the deviation from strictly force-free conditions, deviations from monopole geometry, and/or lack of resolution. Our above results suggest that the BZ mechanism is likely operating in our system, as we concluded in Refs. [26,129].

Roughly 3×10^{-2} of the total initial mass escapes the system after steady state in Mag and Mag + Rad-Full cases and 1.5×10^{-2} of the total mass escapes in the Mag + Rad-Simp case. We estimate that the peak kilonova luminosity and rise time of the case Mag + Rad-Simp are $\approx 10^{41.5}$ erg s⁻¹ and $\approx 9.6 hours$, respectively. For Mag + Rad-Full, the peak kilonova luminosity reaches $\approx 10^{41.6}$ erg s⁻¹ at around $\approx 11.1 h$. Moreover, we estimate that the peak kilonova luminosity, the rise time, and the peak temperature for the magnetized cases are similar to those in the unmagnetized cases (see Table II).

C. GW signals

Figure 8 displays the dominant l = m = 2 mode of the GW strain h_+ versus time, shifted by $t_{\rm merge}$ for the unmagnetized (top panel) and the magnetized (bottom panel) cases. Vertical lines mark the neutrino insertion and BH formation time, respectively. We note that during the inspiral the GW amplitude difference between these cases is $\lesssim 3\%$, with the peak amplitudes shifted by $\sim 80 M \sim 1$ ms. This result is anticipated because the seed magnetic field is initially dynamically unimportant. Following merger, nonaxisymmetric rotation and oscillation modes of the HMNS, which persist until stellar collapse to a BH, trigger the emission of quasiperiodic GWs. We observe that dissipation of energy and angular momentum due to GW radiation is more efficient in the unmagnetized cases, where the GW amplitude is a factor of \sim 1.5 larger than that in the magnetized cases. As pointed out in Ref. [96], magnetic turbulence is an efficient mechanism in damping differential rotation and driving the system into an almost axisymmetric configuration. We also note that neutrino transport of angular momentum (see Fig. 5) enhances the triggering the stellar collapse to a BH.

Figure 9 displays the power spectrum at a distance of 50 Mpc for all cases in Table II along with the sensitivity curves ZERO_DET_HIGH_P for aLIGO, A^+ , and ET in Ref. [145]. The spectra show three distinctive peaks, which were previously referred to as f_{2-0} , $f_{\rm peak}$, and f_{2+0} in Refs. [146,147] and also studied in Refs. [96,148–150]. It has been suggested that the most prominent peak, $f_{\rm peak}$, is due to the rotation of the bar-deformed HMNS [151]. However, the origins of f_{2-0} and f_{2+0} are still debatable. One possible explanation of the origin of f_{2-0} is the nonlinear interaction between the quadrupole and quasiradial modes, and f_{2+0} is the result of the nonlinear interaction of $f_{\rm peak}$ with other nonquasiradial modes

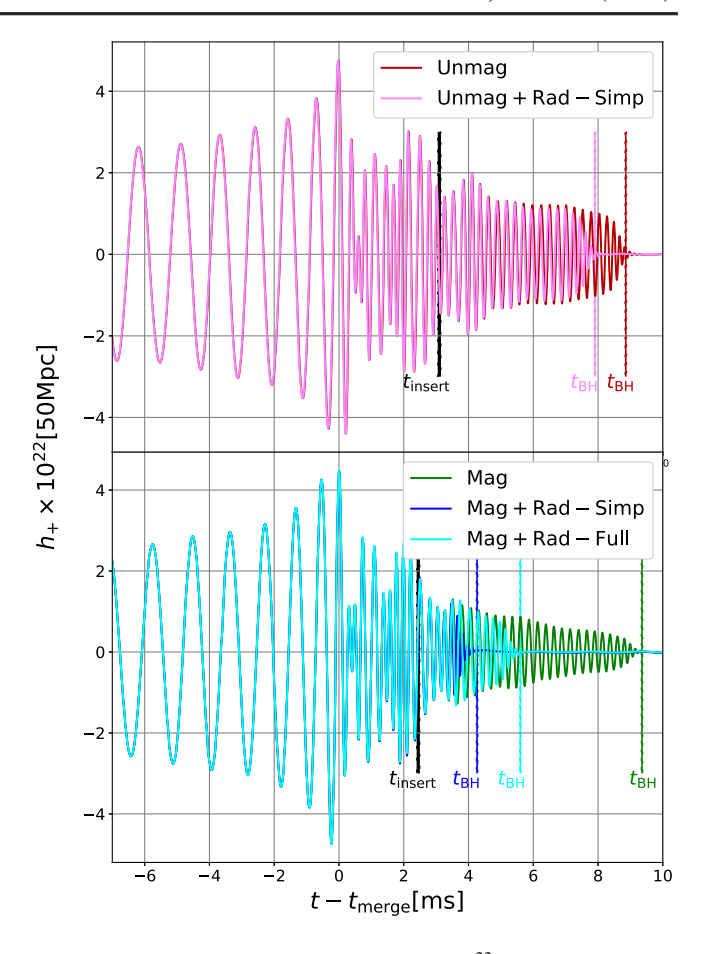


FIG. 8. GW strain of the dominant mode h_+^{22} for unmagnetized (top panel) and magnetized (bottom panel) cases at a source distance of 50 Mpc. Vertical lines mark the neutrino insertion (Mag + Rad cases) and BH formation times.

[151]. Another possible origin of these two modes is the nonlinear oscillations of the two repeatedly colliding and bouncing stellar cores [149]. As a result, it is expected that $f_{\text{peak}} \approx (f_{2-0} + f_{2+0})/2$ for typical HMNS remnants [149]. In our cases, we note that the three peaks $(f_{2-0}, f_{\text{peak}}, f_{2+0})$ are located at $(2.8 \pm 0.05, 3.8 \pm 0.1, 4.7 \pm 0.1 \text{ kHz})$ and hence roughly agree with this relation. Moreover, the location of f_{peak} agrees with the rotation half-period of the bar mode in HMNS at \sim 0.26 \pm 0.02 ms, confirming the bar-mode origin of $f_{\rm peak}$. We also note that the main frequency f_{peak} in the unmagnetized cases is well above the sensitivity curve of aLIGO, and therefore it may be detected with the current sensitivity. By contrast, the main frequency in the magnetized cases is only marginally above it. The other peak frequencies are either marginally above or below the sensitivity curve of aLIGO. These results suggest that the next-generation GW observatories, such as A^+ or the ET (see Fig. 9), are required to characterize the GW signals from GW170817-like remnant events. Furthermore, the majority of the spectrum between 0 and 5 kHz can be detected by both A^+ and the ET, which suggests the potential successful detection of such a source.

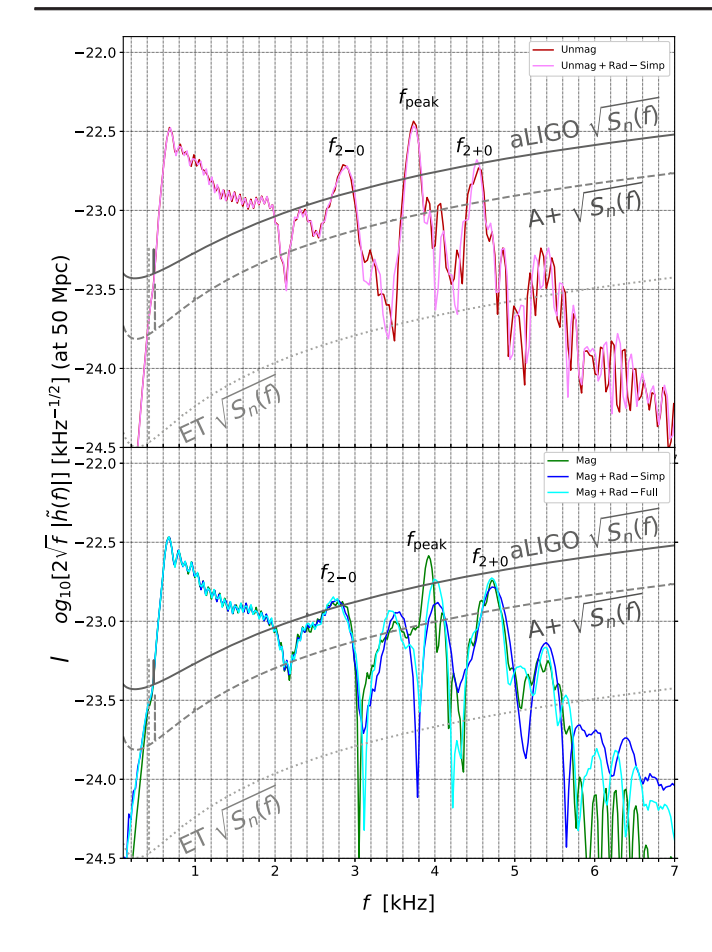


FIG. 9. GW power spectrum of the dominant mode (l,m)=(2,2) at a distance of 50 Mpc for unmagnetized (top panel) and magnetized (bottom panel) cases. The solid-dark, dashed-, and dotted-light gray curves displays the noise sensitivity curves of aLIGO (ZERO_DET_HIGH_P configuration), A^+ , and the Einstein Telescope (ET-D) [152], respectively. Main spectral frequencies are denoted as $f_{\rm peak}$ and $f_{\rm 2\pm0}$.

As shown in the top panel in Fig. 9, the spectra of the two unmagnetized cases show a high resemblance, with several lower dips in the Unmag + Rad-Simp cases as a result of the slightly shorter HMNS lifetime. The main peak f_{peak} for the Mag case lies above aLIGO noise curve, while the two cases with neutrinos have significantly reduced main peaks. On the other hand, the f_{2-0} and f_{2+0} peaks are relatively well preserved. This suggests that the reduced ringdown phase in the neutrino cases may have a contribution to f_{peak} but has little impact on the other two peaks. The relationship between the ringdown waveform and f_{peak} can also be inferred from comparing our waveforms with the results of the generalrelativistic hydrodynamics simulations in Refs. [149,150] with the SLy EOS and an initial NS mass of 1.35 of M_{\odot} . We find that the frequencies of the three peaks in their models are roughly consistent with our unmagnetized cases.

We also assess if any signature of the magnetic field or neutrino radiation can be observed in the GWs. For this, we compute the match function \mathcal{M}_{GW} defined in Ref. [153]

$$\mathcal{M}_{\text{GW}} = \max_{(\phi_c, t_c)} \frac{\langle h_1 | h_2(\phi_c, t_c) \rangle}{\sqrt{\langle h_1 | h_1 \rangle \langle h_2 | h_2 \rangle}}, \tag{36}$$

where $\langle h_1 | h_2 \rangle$ is the noise-weighted inner product defined as [153]

$$\langle h_1 | h_2 \rangle = 4 \operatorname{Re} \int_0^\infty \frac{\tilde{h}_1(f) \tilde{h}_2^*(f)}{S_h(f)} df, \tag{37}$$

where $h=h_+-ih_\times$, \tilde{h} is the Fourier transform of the strain amplitude $\sqrt{\tilde{h}_+(f)^2+\tilde{h}_\times(f)^2}$ of the dominant mode (l,m)=(2,2), and $S_h(f)$ is a given detector sensitivity. We note that the value of $\mathcal{M}_{\rm GW}$ at which two GW waveforms can be distinguishable potentially by instruments depends on the signal-to-noise ratio (SNR). In particular, two signals are indistinguishable when $\mathcal{M}_{\rm GW}\gtrsim 0.9978$ for a SNR of 15 or when $\mathcal{M}_{\rm GW}\gtrsim 0.9992$ for a SNR of 25 [154]. Using the sensitivity curves in Ref. [155] and assuming a source distance of 50 Mpc, we find the following:

- (i) $\mathcal{M}_{\rm GW} = 0.9708$ between Unmag and Mag with a SNR of ~3 for aLIGO, ~1 for KAGRA, ~7 for A^+ , and ~30 for ET.
- (ii) $\mathcal{M}_{GW} = 0.9998$ between Unmag and Unmag + Rad-Simp with a SNR of ~ 3 for aLIGO, ~ 1 for KAGRA, ~ 7 for A^+ , and ~ 30 for ET.
- (iii) $\mathcal{M}_{GW} = 0.9993$ between Mag and Mag + Rad-Simp with a SNR of ~3 for aLIGO, ~1 for KAGRA, ~7 for A^+ , and ~30 for ET.
- (iv) $\mathcal{M}_{\rm GW} = 0.9989$ between Mag and Mag + Rad-Full with a SNR of \sim 3 for aLIGO, \sim 1 for KAGRA, \sim 7 for A^+ , and \sim 30 for ET.

Notice that a SNR of ~ 30 requires a GW event at a distance of ~ 2 Mpc for KAGRA, ~ 6.0 Mpc for aLIGO, or ~ 12.0 Mpc for A^+ . GW170817, the closest GW signal detected to date, had a luminosity distance of 40^{+8}_{-14} Mpc [1]. Therefore, it is unlikely that the current GW detectors can discern any signature from magnetic fields or neutrinos. However, next-generation observatories (e.g., ET) can easily observe their imprints on the GWs.

D. Neutrino emission

We calculate the angular momentum carried off by neutrinos after merger. Our numerical results suggest that the angular momentum loss due to neutrino emission is negligible. Figure 10 shows the evolution of each component of angular momentum as a function of $\Delta t = t_{\rm ret} - t_{\rm BH}$ for Mag + Rad-Full (see Table I). The quantities are measured on a spherical surface with coordinate radius $R=300M\approx 1200$ km. We observe that the angular momentum carried off by neutrinos ΔJ_{ν} is less than 1% of the total angular momentum $J_{\rm int}$ and less than 10% of angular momentum loss due to GW radiation and escaping fluid matter. In the other two remaining cases, ΔJ_{ν} is even

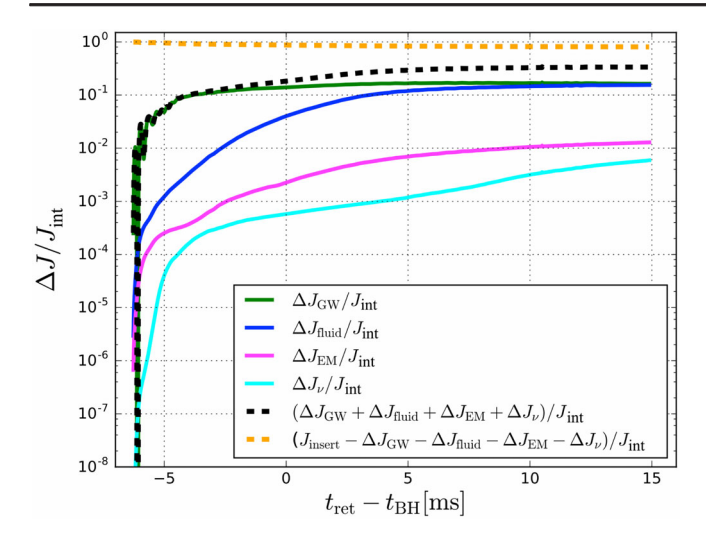


FIG. 10. Different components of angular momentum as functions of $\Delta t = t_{\rm ret} - t_{\rm BH}$ for Mag + Rad-Full, measured on a spherical surface with coordinate radius $R = 300 M \approx 1200$ km. Here, $J_{\rm int}$ is the total interior angular momentum, and $\Delta J_{\rm GW}$, $\Delta J_{\rm fluid}$, $\Delta J_{\rm EM}$, and ΔJ_{ν} denote the angular momentum carried by GWs, fluid, electromagnetic fields, and neutrinos, respectively.

smaller as shown in Table II. Therefore, we conclude that angular momentum loss due to neutrinos is negligible. This result is consistent with the calculation in Ref. [156], in which it has been found that the emission of neutrinos is very inefficient in carrying off angular momentum and may even increase the angular momentum if the polytropic index is less than the critical value 0.45 for a slowly rotating NS. For rapidly rotating stars, the critical polytropic index may increase. In our simulations, the SLy EOS is parametrized with polytropic indices ranging between 0.48–0.55 [90], which is close to the critical value. Therefore, it is expected that neutrino emission has negligible effect on carrying off angular momentum. Moreover, we find that the angular momentum loss rate $d\Delta J_{\nu}/dt$ is around 10^{48} g cm² s⁻², which agrees with the estimate in Ref. [51] using the general-relativistic momentum formalism [48]. Note that Fig. 10 also displays the quantity $J_{\rm insert} - \Delta J_{\rm GW} - \Delta J_{\rm fluid} - \Delta J_{\rm EM} - \Delta J_{\nu}$, where J_{insert} is the total angular momentum J_{int} at t_{insert} , to track the conservation of the total interior angular momentum $J_{\text{int}}(t) = J_{\text{insert}} - \Delta J_{\text{GW}} - \Delta J_{\text{fluid}} - \Delta J_{\text{EM}} - \Delta J_{\nu}.$ observe that $J_{\rm int}$ is conserved within $\sim 1\%$ after the system reaches a steady state.

Figure 11 displays the luminosities of $\bar{\nu}_e$ in Rad-Simp cases and of the three species in Mag + Rad-Full as a function of $\Delta t = t_{\rm ret} - t_{\rm BH}$. The luminosities are measured on a sphere with coordinate radius $R = 300M \approx 1200$ km. We observe that the $\bar{\nu}_e$ neutrino luminosity in Unmag + Rad-Simp peaks at $\Delta t = 0$ with the value $\sim 3 \times 10^{52}$ erg s⁻¹. Then, it gradually decreases, reaching a steady-state value of $\sim 10^{52}$ erg s⁻¹. By contrast, the neutrino luminosity in Mag + Rad-Simp peaks at

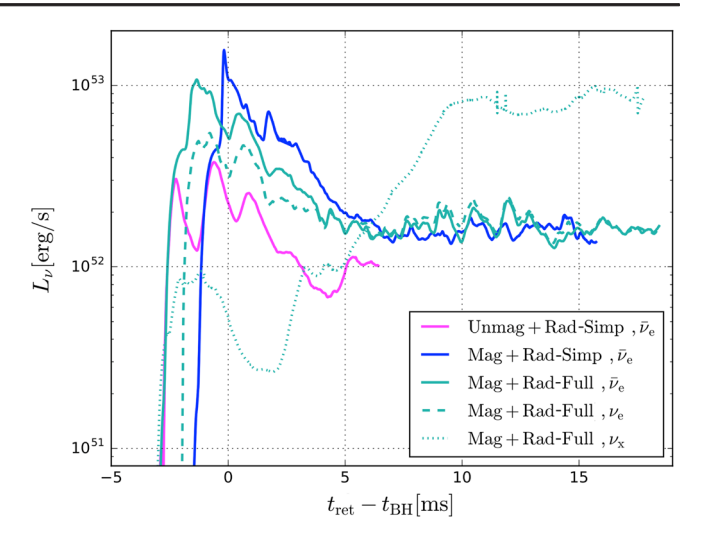


FIG. 11. Neutrino luminosities for the different neutrino species for Rad cases in Table II as a function of $\Delta t = t_{\rm ret} - t_{\rm BH}$. The luminosities are measured at radius $R = 300 {\rm M} \approx 1200 {\rm ~km}$.

 $\sim 2 \times 10^{53} \text{ erg s}^{-1}$ at $\Delta t \approx 135 M \sim 1.8 \text{ ms}$ and settles down at $\sim 2 \times 10^{53}$ erg s⁻¹ at $\Delta t \gtrsim 450 M \gtrsim 6$ ms. This difference in the luminosity is likely due to the turbulent magnetic viscosity, which raises the temperature in the HMNS and the disk, increasing the number and energy of neutrinos. Similarly, the luminosities of $\bar{\nu}_e$ and ν_e in Mag + Rad-Full show analogous behavior to that in Mag + Rad-Simp due to a similar thermal environment. However, we observe that the luminosity of ν_x behaves differently in the two cases, starting to rise quickly at $\Delta t \approx 300 M \approx 4$ ms and reaching a peak value of $\sim 10^{53} \text{ erg s}^{-1}$ at $\Delta t \approx 750 M \approx 10 \text{ ms}$. Differences between the two electron-type neutrinos are negligible compared to differences between the electrontype and heavy-lepton neutrinos. Similar behavior has been also reported in Ref. [54]. The dominance of the scattering opacity over the absorption opacity in a large region of the system may cause a significant uncertainty in the heavylepton neutrinos luminosity. Because of the analytic closure scheme, the neutrino diffusion rate depends heavily on the choice of energy spectrum, which depends on the fluid temperature. Nevertheless, the electron-type neutrino luminosity obtained in our cases broadly agrees with previous M1 and MC studies [54,157].

V. CONCLUSIONS

To understand multimessenger observations, numerical simulations of compact binary mergers involving magnetic fields, neutrinos, and detailed microphysics are required. As another step toward this goal, we reported here our implementation of a radiative transport scheme for neutrino processes in our Illinois GRMHD code. This implementation uses the general-relativistic, truncated moment formalism in which the first two moments of radiation, i.e., energy density E and the fluxes F^{α} , are evolved. To close the

evolution equations, the radiation stress $\mathcal{P}^{\alpha\beta}$ is interpolated between the optically thick and thin limits using the analytic expression in Ref. [83] (see the current paper's Appendix A). The code has been tested in multiple regimes, including those handled by our earlier radiation-GRMHD code in Ref. [80]. Here, we presented the nontrivial, strong gravity test of "thermal Oppenheimer-Snyder collapse" in Appendix F to assess its capability of evolving radiation fields and computing interactions between radiation and matter in optically thick, thin, and transition regions in a strong gravitational field containing matter and a BH.

We used this radiation evolution module to incorporate neutrino interactions in GRMHD simulations of NSNS mergers that undergo delayed collapse to a BH. In particular, we considered binaries modeled using a piecewise representation of the cold SLy nuclear EOS previously reported in Ref. [96], augmented by a nonzero temperature contribution appropriate for semidegenerate neutrons. The neutrinos are inserted shortly after the binary merger $(t - t_{\text{merge}} \sim 225 M \sim 3 \text{ ms})$. To probe the effects of neutrino radiation, we adopted two version for the microphysics. In the first warm-up version, denoted as Rad(Sim), we only considered the interactions of $\bar{\nu}_e$, setting the electron fraction $Y_e = 0$. In the second version, denoted as Rad-Full, we evolved three neutrino species ν_e , $\bar{\nu}_e$, and ν_r and their antineutrinos and took all related interactions into account. We found that during the HMNS phase, the remnant is subjected to an effective viscosity due to turbulent magnetic fields, which induces the formation a massive central core surrounded by a Keplearian cloud of matter. We noted that the MRI would not be affected by neutrino-induced effective viscosity and drag forces as discussed earlier [44], since in our simulations the magnetic field in the HMNS is $B \gtrsim 10^{15}$ G and exceeds a critical field strength. However, our simulations indicate that neutrino advective transport may assist in reducing the differential rotation of the HMNS. These processes reduce the lifetime of the remnant by $\gtrsim 4$ ms compared to that in the neutrino-free cases.

Following BH formation, we observed that the BH remnants are more massive and have higher spins when neutrinos are included, while the disk accretion rate $(\dot{M} \sim 2~{\rm M}_{\odot}/{\rm s})$ and the fraction of escaping mass $(M_{\rm esc} \sim 8 \times 10^{-3}~M_{\odot})$ show no noteworthy differences after a quasisteady state is achieved. We note that the latter is roughly consistent with the ejecta mass reported by a previous hydrodynamic SPH simulation of NSNS mergers with a neutrino leakage scheme [41], as well as another GRMHD simulation of NSNS mergers [119,120]. We also estimated the peak kilonova luminosity, the rise time, and the effective temperature/wavelength inferred by our simulations and concluded that the signals may be observed by current or future instruments such as ALMA or the Vera C. Rubin observatory [123,124].

In all cases, a magnetically supported jet is launched after $t - t_{\rm BH} \gtrsim 750 M \gtrsim 10$ ms. However, neutrino processes reduce the baryon-loaded environment in the polar region above the BH poles, allowing the emergence of the jet $\sim 1000 M \sim 15$ ms earlier than in cases without neutrinos. The disk accretion time (jet's fuel) is ~ 0.1 s, which is consistent with the lifetime of the sGRBs central engine. We also found strong evidence that the Blandford-Znajek mechanism for launching jets is operating in our systems.

In our simulations, we found that neutrinos are inefficient in carrying off angular momentum, which is in agreement with previous analytic studies [156]. The angular momentum loss rate due to neutrino emission is $\sim 10^{48}$ g cm² s⁻², which is consistent with the previous GR simulations [51]. We found that neutrino luminosity is approximately 10^{52-53} erg s⁻¹ in our cases, which agrees with the previous compact binary merger simulations using M1 or MC transport methods [54,157].

To probe if magnetic field and neutrino signatures can be observed by current and/or future GW observatories, we computed the GW power spectrum of the dominant mode assuming a source distance of 50 Mpc. We found that only its main frequency f_{peak} is well above the sensitivity curves of aLIGO and A+. By contrast, in the magnetized cases, the other key frequencies are at most marginally above these curves. These results suggest that only next-generation GW observatories, such as the Einstein Telescope, are required to characterize fully the GW signals from the remnant of GW170817-like events. In addition, we computed the match function between waveforms from systems with different magnetic field and neutrino content. We found that at a distance of 50 Mpc only the next generation of ground-based GW detectors, such as the Einstein Telescope, can observe imprints of the magnetic field and neutrinos.

We also realize several limitations to our implementation and suggest some future improvements. First, the calculation of temperature is based on an approximate analytic expression, which in turn determines the net-electron fraction, opacities, and emissivities. Currently several more realistic, finite-temperature EOSs have been proposed. They are based on a finite-temperature liquid drop model with a Skyrme nuclear force [158], on the relativistic meanfield model extended with the Thomas-Fermi approximation [159], or on a statistical model that consists of an ensemble of nuclei and interacting nucleons in nuclear statistical equilibrium [160]. These EOSs are in tabular form, which is rendered as functions of baryon density, temperature, and the net electron fraction. We hope to implement these in future investigations. Also, even though the M1 method provides a reasonable first approximation to radiative transport [50], neutrino luminosities and the outflow composition have a non-negligible dependence on the analytic closure schemes [53,161]. Moreover, the energy-integrated M1 scheme is unable to provide information about the neutrino energy spectrum. However, an energy-dependent transport scheme is computationally expensive for a full merger simulation, especially when magnetic fields are present. Monte Carlo techniques have been used in neutron star simulations [54] and have been found to yield results similar to those of M1 schemes. The major disagreement comes from the luminosity of heavy-lepton neutrinos. In regions where heavy lepton neutrinos have high scattering and low absorption opacities, the M1 scheme has greater errors due to the difficulty of predicting the correct neutrino energy spectrum. We hope to explore improvements to our neutrino scheme in the future.

ACKNOWLEDGMENTS

We thank T. Baumgarte, F. Foucart, and J. Noronha-Hostler for several useful discussions. We also thank members of the Illinois Relativity Undergraduate Research Team (M. Kotak, J. Huang, E. Yu, and J. Zhou) for assistance with some of the visualizations. This work was supported in part by National Science Foundation Grant No. PHY-2006066 and the NASA Grant No. 80NSSC17K0070 to the University of Illinois at Urbana-Champaign. L. S. thanks also The Illinois Center for Advanced Studies of the Universe (ICASU) for financial support. This work made use of the Extreme Science and Engineering Discovery Environment (XSEDE), which is supported by National Science Foundation Grant No. TG-MCA99S008. This research is part of the Frontera computing project at the Texas Advanced Computing Center. Frontera is made possible by National Science Foundation Grant No. OAC-1818253. Resources were also provided by the NASA High-End Computing Program through the NASA Advanced Supercomputing Division at Ames Research Center. This research is also part of the Blue Waters sustained-petascale computing project, which is supported by the National Science Foundation (Awards No. OCI-0725070 and No. ACI-1238993) and the State of Illinois. Blue Waters is a joint effort of the University of Illinois at Urbana-Champaign and its National Center for Supercomputing Applications.

APPENDIX A: RADIATION CLOSURE SCHEME

We compute the radiation pressure using the M1 closure scheme, which is an interpolation between the optically thin and optically thick limits. Following Refs. [48,50], we express the radiation pressure terms as

$$\mathcal{P}^{\alpha\beta} = \frac{3\chi(\zeta) - 1}{2} \mathcal{P}_{\text{thin}}^{\alpha\beta} + \frac{3[1 - \chi(\zeta)]}{2} \mathcal{P}_{\text{thick}}^{\alpha\beta}, \quad (A1)$$

where the factor χ is given by the Minerbo closure function [83]

$$\chi(\zeta) = \frac{1}{3} + \zeta^2 \frac{6 - 2\zeta + 6\zeta^2}{15},\tag{A2}$$

where the quantity $\zeta = F^{\alpha}F_{\alpha}/E^2$, with F^{α} the radiation flux and E the radiation energy density. We note that ζ goes to 0 in the optically thick region and to 1 in the optically thin region. The optically thick limit of radiation pressure is given by [80]

$$\mathcal{P}_{\text{thick}}^{\alpha\beta} = \frac{E}{3} h^{\alpha\beta},\tag{A3}$$

where $h^{\alpha\beta}=g^{\alpha\beta}+u^\alpha u^\beta$ is the projection tensor onto the orthogonal slices of the fluid 4-velocity. In the optically thin limit, we have

$$P_{\text{thin}}^{\alpha\beta} = \frac{F^{\alpha}F^{\beta}}{F^{\mu}F_{\mu}}E. \tag{A4}$$

Note that, Eq. (A4) reduces to the form adopted in Ref. [50] in asymptotically flat spacetimes, which is satisfied in our simulations at a large distance from our binaries.

APPENDIX B: RECOVERING PRIMITIVE VARIABLES

The evolution of the radiation conservative variables $(\bar{\tau}, \bar{S}_i)$ [see Eqs. (15) and (17)] involves the calculation of the radiation primitive variables (E, F^i) at each iteration, which in turn requires a 4×4 root finder given the closure expressions (A1) and (A2). In our code, we use a Newton-Raphson solver to find the roots of the set of functions $f_u(E, F^i)$,

$$f_i = \alpha \sqrt{\gamma} [Eu^0 u_i + F^0 u_i + F_i u^0 + \mathcal{P}_i^0] / \bar{S}_i - 1,$$
 (B1)

and

$$f_4 = (\alpha^2 \sqrt{\gamma}) [E(u^0)^2 + 2F^0 u^0 + \mathcal{P}^{00}]/\bar{\tau} - 1,$$
 (B2)

where \bar{S}_i and $\bar{\tau}$ are computed at a given iteration, while E and F^i are known values at the previous iteration. We apply the Newton-Raphson method to solve for the set of equations $f_{\mu}(E,F^i)=0$. The solver returns the primitive variables (E,F^i) as values at the current iteration when all four functions reduce below the tolerance $f_{\mu}<10^{-12}$.

The first-order Newton-Raphson method requires a matrix of partial derivatives, namely, the Jacobian

$$J_{f} = \begin{bmatrix} \frac{\partial \bar{S}_{i}}{\partial F_{j}} & \frac{\partial \bar{S}_{i}}{\partial E} \\ \frac{\partial \bar{\tau}}{\partial F_{j}} & \frac{\partial \bar{\tau}}{\partial E} \end{bmatrix}, \tag{B3}$$

in which the derivatives can be evaluated analytically. The specific components of J_f are

$$\frac{\partial \bar{\tau}}{\partial E} = \alpha^2 \sqrt{\gamma} \left\{ \frac{4(u^0)^2}{3} + (A - B\zeta) \right\}
\left[\frac{(F^0)^2}{F^{\alpha}F_{\alpha}} - \frac{g^{00} + (u^0)^2}{3} \right] + \frac{g^{00}}{3} ,$$
(B4)

$$\frac{\partial \overline{S_i}}{\partial E} = \alpha^2 \sqrt{\gamma} \left\{ \frac{4u^0 u_i}{3} + (A - B\zeta) \left[\frac{F^0 F_i}{F^\alpha F_\alpha} - \frac{u^0 u_i}{3} \right] \right\}, \quad (B5)$$

$$\begin{split} \frac{\partial \overline{\tau}}{\partial F_i} &= \alpha^2 \sqrt{\gamma} \bigg\{ 2(g^{i0} + v^i g^{00}) \bigg(u^0 + AE \frac{F^0}{F^\alpha F_\alpha} \bigg) \\ &+ (F^i - v^i F^0) \bigg[\frac{B}{\sqrt{F^\alpha F_\alpha}} \bigg(\frac{(F^0)^2}{F^\alpha F_\alpha} - \frac{g^{00} + (u^0)^2}{3} \bigg) \\ &- AE \frac{2(F^0)^2}{(F^\alpha F_\alpha)^2} \bigg] \bigg\}, \end{split} \tag{B6}$$

and

$$\begin{split} \frac{\partial \bar{S}_{j}}{\partial F_{i}} &= \alpha \sqrt{\gamma} \bigg\{ \bigg(u^{0} + \frac{AEF^{0}}{F^{\alpha}F_{\alpha}} \bigg) \delta_{j}^{i} \\ &+ (g^{i0} + v^{i}g^{00}) \bigg(u_{j} + AE\frac{F_{j}}{F^{\alpha}F_{\alpha}} \bigg) \\ &+ (F^{i} - v^{i}F^{0}) \bigg[\frac{B}{\sqrt{F^{\alpha}F_{\alpha}}} \bigg(\frac{F^{0}F_{j}}{f^{\alpha}F_{\alpha}} - \frac{u^{0}u_{j}}{3} \bigg) \\ &- AE\frac{2F_{j}F^{0}}{(F^{\alpha}F_{\alpha})^{2}} \bigg] \bigg\}, \end{split} \tag{B7}$$

where

$$A \equiv \frac{3\chi - 1}{2} = \frac{1}{5} (3\zeta^2 - \zeta^3 + 3\zeta^4), \tag{B8}$$

and

$$B \equiv \frac{1}{5}(6\zeta - 3\zeta^2 + 12\zeta).$$
 (B9)

Once the Jacobian is computed, the solver performs lower upper (LU) decomposition and back substitution in the Jacobian to find the direction of the Newton step. Then, the code uses line searches and backtracking methods (see Sec. 9.7 in ref. [109]) to reduce the number of iterations for convergence. After obtaining (E,F^i) , we impose a floor value of radiation energy density $E_{\rm atm}=10^{-9}E_{\rm max}$ and set the radiation fluxes to zero if $E < E_{\rm atm}$ to reliably evolve in the regions with low radiation energy. Knowing the values of the primitive variables, we then recompute the conserved variables and impose the radiation contributions to the total stress-energy tensor in the BSSN equations.

APPENDIX C: FINITE-TEMPERATURE EOS

To treat neutrinos, it is necessary to evolve NSs with finite-temperature matter. However, in our simulations, we adopt an SLy nuclear EOS to model the cold component and employ an approximate analytic expression for the hot component. Notice that our simplified, analytic method of computing the temperature and the opacity during the NS evolution can be straightforwardly extended to realistic, tabulated, thermal EOSs.

1. Thermal energy density and pressure

Our simplified, analytic hot nuclear EOS assumes that the total nucleon energy density and pressure consists of two parts,

$$\mathcal{E} = \mathcal{E}_{\text{cold}} + \mathcal{E}_{\text{th}},$$
 (C1)

$$P = P_{\text{cold}} + P_{\text{th}},\tag{C2}$$

where $P_{\rm cold}$ and $\mathcal{E}_{\rm cold}$ are the cold pressure. On the other hand, the energy density and the thermal component are given by the sum of the nucleon and thermal radiation components

$$\mathcal{E}_{th} = \mathcal{E}_{nuc} + \mathcal{E}_{rad},$$
 (C3)

$$P_{\rm th} = P_{\rm nuc} + P_{\rm rad}. \tag{C4}$$

The nucleon part of the thermal energy density is based on a semidegenerate, ideal neutron gas expression that limits to a Maxwell-Boltzmann gas in the nondegenerate limit [162]

$$\mathcal{E}_{\text{nuc}} = \frac{3}{2} n k_B T \min \left\{ 1, \frac{2(3\pi^2)^{1/3} m_{\text{nuc}}}{18(\hbar c)^2} n^{-2/3} k_B T \right\}, \quad (C5)$$

where $m_{\rm nuc}$ is the nucleon mass, $n=\rho_0/m_{\rm nuc}$ is the nucleon number density, k_B is Boltzmann's constant, and T is the temperature of the fluid. This expression accommodates both the low-temperature semidegenerate and the high-temperature Maxwell-Boltzmann limits. The thermal nucleon part of the pressure is given by

$$P_{\text{nuc}} = (\gamma - 1)\mathcal{E}_{\text{nuc}},\tag{C6}$$

with $\gamma = 5/3$, as the nucleons are essentially nonrelativistic. We note that in most NSNS merger and postmerger scenarios the second term in the brackets in Eq. (C5) is greater than or comparable to 1 throughout the matter. Therefore, for simplicity, we typically can adopt the simpler expression $\mathcal{E}_{\text{nuc}} = (3/2)nk_BT$. The "radiation" part of the energy density includes photons and relativistic

electron and positron pairs and follows a Stefan-Boltzmann relation, ¹

$$\mathcal{E}_{\rm rad} = \mathcal{E}_{\rm ph} + \mathcal{E}_{\rm pair} = \left(1 + \frac{7}{4}\right) a T^4 = \frac{11}{4} a T^4,$$
 (C7)

and

$$P_{\rm rad} = \frac{1}{3} \mathcal{E}_{\rm rad}.$$
 (C8)

Combining nucleon and radiation components, the thermal energy density and pressure, we typically can adopt the simplification

$$\mathcal{E}_{\text{th}} = \frac{3}{2}nk_B T + \frac{11}{4}aT^4,$$
 (C9)

$$P_{\rm th} = nk_B T + \frac{11}{12}aT^4.$$
 (C10)

2. Numerical implementation

After the update of rest-mass density ρ_0 and the total specific internal energy ϵ at each iteration, we obtain the thermal part of the specific internal energy according to

$$\epsilon_{\rm th} = \epsilon - \epsilon_{\rm cold}$$
 (C11)

and the thermal energy density as

$$\mathcal{E}_{\rm th} = \rho_0 \epsilon_{\rm th}.\tag{C12}$$

The cold part of the specific internal energy and pressure for SLy can be modeled by a four-piece piecewise polytropic EOS:

$$P_{\text{cold}}^{i} = \kappa^{i} \rho_{0}^{\Gamma_{i}}, \tag{C13}$$

$$\epsilon_{\text{cold}}^{i} = \frac{P_{\text{cold}}^{i}}{\rho_{0}(\Gamma_{i} - 1)} = \frac{\kappa^{i} \rho_{0}^{\Gamma_{i} - 1}}{\Gamma_{i} - 1}.$$
 (C14)

Here, κ_i and Γ_i are the corresponding polytropic constant and the polytropic exponent of the rest-mass density in the range $\rho_{0,i-1} \leq \rho_0 \leq \rho_{0,i}$, respectively [90]. Once the thermal energy density is computed, we use Eqs. (C9) and (C10) to compute the temperature and the thermal pressure.

We use the HARM 2D primitive solver to compute the MHD variables [163,164]. It finds roots of a two-dimensional system with variables

$$v^2 \equiv v_i v^i, \tag{C15}$$

and

$$W = w\gamma^2 = \frac{\rho_0(1 + \epsilon + P/\rho_0)}{1 - v^2}.$$
 (C16)

In this setup, the total pressure P needs to be expressed as functions of v^2 and W, while the derivatives dP/dW and dP/dv^2 are needed for the Jacobian. Let us begin with the temperature-dependent thermal pressure and energy density. Simple algebraic manipulations of Eqs. (C9) and (C10) yield

$$\rho_0 \epsilon_{\text{th}} = 3P_{\text{th}} - 1.5nT = 3(P - P_{\text{cold}} - 0.5T).$$
 (C17)

Next, using Eq. (C16), we obtain

$$P = 0.25 \quad [W(1-v^2) - \rho_0(1+\epsilon_{\rm cold}) + 3P_{\rm cold} + 1.5nT]. \eqno(C18)$$

From Eq. (C18), we calculate the derivatives

$$\frac{dP}{dW} = 0.25(1 - v^2),\tag{C19}$$

and

$$\begin{split} \frac{dP}{dv^2} &= 0.25 \left[\left(-1 - \epsilon_{\text{cold}} + (3\Gamma_i - 1) \frac{P_{\text{cold}}}{\rho_0} \right) \frac{d\rho_0}{dv^2} \right. \\ &+ 1.5 \frac{d(nT)}{dv^2} - W \right]. \end{split} \tag{C20}$$

in which the derivative $d(nT)/dv^2$ is given by

$$\frac{d(nT)}{dv^{2}} = \frac{T}{m_{n}} \frac{d\rho_{0}}{dv^{2}} + \frac{\rho_{0}}{m_{n}} \frac{dT}{dv^{2}}
= \frac{T}{m_{n}} \frac{d\rho_{0}}{dv^{2}} + \frac{\rho_{0}}{m_{n}} \left(\frac{dT}{d\rho_{0}} \frac{d\rho_{0}}{dv^{2}}\right).$$
(C21)

The first term in Eq. (C21) can be computed directly. To find the second term, we begin setting the radiation constant a=1 in the thermal pressure (Eq. (C10), and by taking a derivative with respect to the temperature, we have

$$\frac{dP_{\rm th}}{dT} = \frac{11}{3}T^3 + \frac{\rho_0}{m_{\rm tr}}.$$
 (C22)

Next, we express dP_{th}/dT using P and P_{cold} as

$$\frac{dP_{\rm th}}{dT} = \frac{dP_{\rm th}}{d\rho_0} \frac{d\rho_0}{dT} = \left(\frac{dP}{d\rho_0} - \frac{dP_{\rm cold}}{d\rho_0}\right) \frac{d\rho_0}{dT},\tag{C23}$$

¹Note that electron-positron pairs become relativistic and the $7aT^4/4$ is appropriate only when $k_BT > 2m_ec^2 \sim 1$ MeV. However, in NSNS mergers, the temperature is typical $\gtrsim 10$ MeV, and hence we always keep this term.

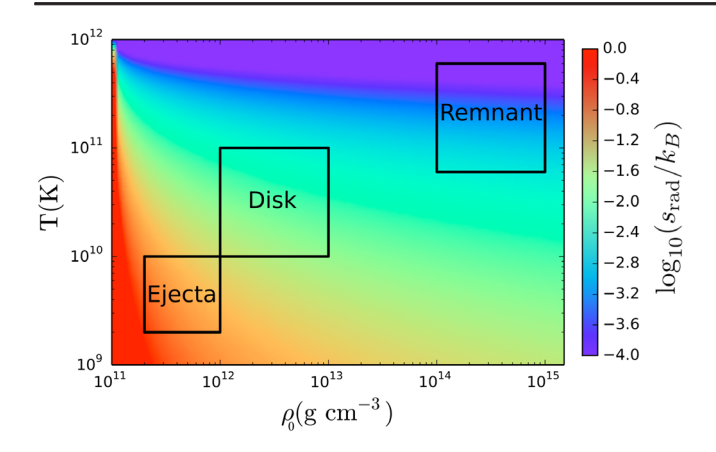


FIG. 12. Ratio $s_{\rm rad}/k_B$ (log scale) as a function of ρ_0 and T. The boxes show the parameter space typical for the NSNS remnant, accretion disk, and ejecta.

and

$$\frac{dP}{d\rho_0} = \frac{dP}{dW}\frac{dW}{d\rho_0} = \frac{dP}{dW}\left(\frac{1}{1-v^2}\frac{dw}{d\rho_0}\right)$$

$$= 0.25 \left[\frac{d(\rho_0 + \rho_0\epsilon + P)}{d\rho_0}\right], \quad (C24)$$

where we used Eq. (C19) for dP/dW. Expanding this equation, we obtain

$$3\left(\frac{dP}{d\rho_0}\right) = 1 + \rho_0 \left[\frac{d(\epsilon_{\rm cold} + \epsilon_{\rm th})}{d\rho_0}\right] + \epsilon_{\rm cold} + \epsilon_{\rm th}.$$
 (C25)

On the other hand, taking the derivative of the thermal energy density (Eq. (C9) with respect to temperature and using Eq. (C12), we find

$$\frac{d\epsilon_{\rm th}}{d\rho_0} = \frac{1}{\rho_0} \left(11T^3 + 1.5 \frac{\rho_0}{m_n} - \frac{d\rho_0}{dT} \epsilon_{\rm th} \right) \frac{dT}{d\rho_0}.$$
 (C26)

Inserting the above expression in Eq. (C25), we find

$$3\left(\frac{dP}{d\rho_0}\right) = 1 + \rho_0 \left(\frac{d\epsilon_{\text{cold}}}{d\rho_0}\right) + \epsilon_{\text{cold}} + \left(11T^3 + 1.5\frac{\rho_0}{m_n}\right) \frac{dT}{d\rho_0}.$$
 (C27)

The last term in this equation can be computed using $dP/d\rho_0$ in Eq. (C23) and equating it with Eq. (C22),

$$\frac{d\rho_0}{dT} = \frac{1.5\frac{\rho_0}{m_n}}{1 + \epsilon_{\text{cold}} + (1 - 3\Gamma_i)\frac{P_{\text{cold}}}{\rho_0}},$$
 (C28)

which allow us to compute the second term in Eq. (C21). Finally, we use Eq. (C20) to get

$$\frac{dP}{dv^2} = 0.25 \left(-W + 1.5 \frac{T}{m_n} \frac{d\rho_0}{dv^2} \right),$$
 (C29)

which completes the derivative terms in the Jacobian of the finite-temperature HARM 2D solver.

3. Sound speed

The sound speed of the fluid c_s can be obtained using the derivative of P with respect to ρ_0 at constant entropy $c_s^2 = (dP/d\rho_0)/h|_s$, where h is the specific enthalpy. Using the relations in Eqs. (C4), (C6), and (C8), we have

$$c_{\rm s}^2 = \frac{1}{h} \left(\frac{dP_{\rm cold}}{d\rho_0} + \frac{dP_{\rm nuc}}{d\rho_0} + \frac{dP_{\rm rad}}{d\rho_0} \right)_{\rm s}, \quad (C30)$$

where

$$\frac{dP_{\text{cold}}}{d\rho_0} = \Gamma_i \frac{P_{\text{cold}}}{\rho_0},\tag{C31}$$

$$\frac{dP_{\text{nuc}}}{d\rho_0} = \frac{\partial P_{\text{nuc}}}{\partial \rho_0} + \frac{\partial P_{\text{nuc}}}{\partial T} \frac{dT}{d\rho_0} \bigg|_{s}, \tag{C32}$$

and

$$\frac{dP_{\rm rad}}{d\rho_0} = \frac{\partial P_{\rm rad}}{\partial T} \frac{dT}{d\rho_0} \bigg|_{\rm s}.$$
 (C33)

The term $(dT/d\rho_0)|_{\rm s}$ is calculated by using the isentropic condition, where the total entropy per baryon $s_{\rm tot} = s_{\rm nuc} + s_{\rm rad}$ is constant, or $ds_{\rm tot} = ds_{\rm nuc} + ds_{\rm rad} = 0$. From Eqs. (C9) and (C10), we obtain

$$s_{\text{nuc}} = k_B \left[\frac{5}{2} + \ln \left[\frac{1}{n} \left(\frac{m_B k T}{2\pi \hbar^2} \right)^{3/2} \right] \right],$$
 (C34)

and

$$s_{\rm rad} = \frac{11}{3} \frac{m_B}{\rho_0} a T^3,$$
 (C35)

which gives

$$ds_{\text{nuc}} + ds_{\text{rad}}$$

$$= \left[k_B \left(-\frac{dn}{n} \right) + \frac{3}{2} k_B \frac{dT}{T} \right] + \left(11a \frac{T^2 dT}{n} + 11a T^3 \frac{dn}{n^2} \right)$$

$$\left[k_B \left(-\frac{d\rho_0}{\rho_0} \right) + \frac{3}{2} k_B \frac{dT}{T} \right] + \left(3s_{\text{rad}} \frac{dT}{T} - s_{\text{rad}} \frac{d\rho_0}{\rho_0} \right) = 0.$$
(C36)

Simplifying the above, we obtain

$$\frac{dT}{d\rho_0}\Big|_{s} = \left(\frac{2\frac{s_{\text{rad}}}{k_B} + 2}{6\frac{s_{\text{rad}}}{k_B} + 3}\right)\frac{T}{\rho_0} = \sigma_{s2}\frac{T}{\rho_0},$$
 (C37)

where $\sigma_{s2} = (2s_{\rm rad}/k_B + 2)/(6s_{\rm rad}/k_B + 3)$. Applying relation (C37) to (C32) and (C33), the sound speed reads

$$c_{\rm s}^2 = \frac{1}{h} \left[\Gamma_i \frac{P_{\rm cold}}{\rho_0} + \frac{2}{3} \varepsilon_{\rm nuc} (1 + \sigma_{s2}) + \frac{4}{3} \sigma_{\rm s2} \varepsilon_{\rm rad} \right]. \quad (C38)$$

In most regions of the NSNS remnant, the ratio $s_{\rm rad}/k_B$ remains small. As shown in Fig. 12, $s_{\rm rad}/k_B$ stays $\lesssim 10^{-3}$ for the NSNS remnant and $\lesssim 10^{-2}$ in the accretion disk, even though it may reach ~ 0.2 in the ejecta. Hence, for most regions, $\sigma_{s2} \rightarrow 2/3$, which reduces Eq. (C38) to

$$c_{\rm s}^2 \approx \frac{1}{h} \left[\Gamma_i \frac{P_{\rm cold}}{\rho_0} + \frac{10}{9} \varepsilon_{\rm nuc} + \frac{8}{9} \sigma_{\rm s2} \varepsilon_{\rm rad} \right].$$
 (C39)

In our numerical implementation, we approximate the sound speed by

$$c_{\rm s,code}^2 = \frac{1}{h} \left[\Gamma_i \frac{P_{\rm cold}}{\rho_0} + \frac{8}{9} (\varepsilon_{\rm nuc} + \varepsilon_{\rm rad}) \right], \quad (C40)$$

for efficiency. We note that this approximation of the isentropic sound is valid when the ε_{nuc} is smaller than the other two terms in Eq. (12). However, even if ε_{nuc} is larger, the above expression underestimates the sound speed by at most ~20%, which is smaller than the overestimation of computing the characteristic speed c^{\pm} for the HLL Riemann solver using the approximated general GRMHD dispersion relation. According to Ref. [165], compared to the original, full dispersion relation, (Eq. (27) of Ref. [163]), the simplified expression adopted in our code overestimates the maximum characteristic speed by a factor \leq 2. Note that this approximate dispersion relation has been widely used in various codes including Whisky-MHD [166], GRHydro [167], and HARM 3D [168].

APPENDIX D: NEUTRINO SOURCE TERMS

The calculation of the radiation four-force density G^{α} requires three key quantities [see Eq. (14)]: (1) the neutrino emissivity η , (2) the absorption opacity κ_a , and (3) the scattering opacity κ_s . Following Ref. [50], we first compute the absorption opacity of electron neutrinos due to two charged-current interactions, which are the absorption of ν_e onto neutrons according to Eq. (A11) in Ref. [86] (henceforth "RJS") and the absorption of $\bar{\nu}_e$ onto protons according to Eq. (A12) in RJS. The inverse processes of the two interactions are responsible for the emission of electron-type neutrinos. In the optically thick limit, we apply the energy-integrated Kirchhoff law [50]

$$\eta_{\rm Kir} \approx \int_0^\infty \kappa_a B_{\nu}(\varepsilon_{\nu}) d\varepsilon_{\nu} \approx \frac{7}{8} \mathcal{N}_{\nu} \kappa_a a T^4, \qquad (D1)$$

where the specific intensity B_{ν} is the Fermi-Dirac intensity and the absorption opacity κ_a is an energy-averaged (e.g., Rosseland mean) opacity. In the optically thin limit, Eqs. (B1) and (B2) in RJS give the free emission rates of the two charged-current interactions, from which we obtain the emissivity in the free-streaming regime $\eta_{\rm fs}$. Hence, the total emissivity from the charged-current interaction is given by the interpolation between $\eta_{\rm Kir}$ and $\eta_{\rm fs}$ with the same method used to interpolate the radiation stress tensor

$$\eta = \frac{3\chi(\zeta) - 1}{2} \eta_{fs} + \frac{3[1 - \chi(\zeta)]}{2} \eta_{Kir},$$
(D2)

where χ and ζ are defined in Appendix A. We then consider the free emission of three pair processes, including electron pair annihilation, plasmon decay, and nucleon-nucleon bremsstrahlung. RJS gives the emission rate due to pair annihilation and plasmon decay for electron-type neutrinos in their Eqs. (B8) and (B11) and those for heavy-lepton neutrinos in their Eqs. (B10) and (B12). The emission rate for nucleon-nucleon bremsstrahlung is given in Ref. [87]. Note that the expression of the emissivity for the two heavy-lepton species and their antineutrinos $(n_{\mu}, \bar{\nu}_{\mu}, \nu_{\tau})$, and $\bar{\nu}_{\tau}$) are the same, so we can merge the four types of particles as ν_x and evolve them together as a single variable. Next, the inverse of the pair processes contributes to the absorption opacities and is again computed using Kirchhoff's law. Note that, for heavy lepton neutrinos, $\mathcal{N}_{\nu} = 4$ as a result of lumping two species (plus antineutrino) together, while $\mathcal{N}_{\nu} = 1$ for ν_e and $\bar{\nu}_e$. Lastly, we consider the scattering opacities for all species given by Eq. (A6) in RJS.

The calculation of the terms above requires the knowledge of neutrino temperature, nucleon number density, neutrino chemical potential, and net electron fraction, as well as terms such as the Pauli blocking factor. We evolve the nucleon density, while the temperature is computed as in Appendix C. In the following, we summarize our treatment to obtain the other ingredients.

1. Chemical potentials

For the chemical potential of neutrinos, which are used in computing the blocking factors, we adopt the expressions in Ref. [86],

$$\mu_{\nu_e} = \mu_{\nu_e}^{\text{ceq}} [1 - \exp(-\tau_{\nu_e})] + \mu_{\nu_e}^0 \exp(-\tau_{\nu_e}), \quad \text{(D3)}$$

where τ_{ν_e} is the optical depth, which is estimated as the minimum of the line integrals of total opacity along the three Cartesian directions, and $\mu_{\nu_e}^{\rm ceq} = \mu_e + \mu_p - \mu_n - Q$ is the chemical potential of electron neutrinos in chemical equilibrium. Here, Q = 1.2935 MeV $\approx 2 \times 10^{-6}$ erg is the

rest-mass energy difference between a neutron and a proton, and $\mu_{\nu_e}^0$ is the chemical potential in low-density, transparent matter, which, by simplicity, we set to zero. For μ_e , μ_p , and μ_n , we use Eq. (11.2.4) in Ref. [169].

2. Pauli blocking factors

We need to compute the Pauli blocking factor that appears in the absorption and scattering opacities and emissivity in various neutrino processes. They are obtained as integrals over momentum of the Fermi distribution function for the relevant nucleons and electrons involved in the reactions. We adopt expressions for $Y_{\rm NN}$, Y_{np} , Y_n , Y_p , and Y_e obtained in Ref. [170] for equilibrium mixtures. These quantities are defined as follows:

- (i) $Y_{\rm NN}$ defines the phase space fractions of free neutrons (when $N \equiv n$) or protons (when $N \equiv p$), due to the Pauli blocking effects in nucleon scattering reaction [see Eq. (24)].
- (ii) Y_{np} defines the phase space fraction of free nucleons due to the absorption by neutrons [the inverse reaction of Eq. (19)].
- (iii) Y_n , Y_p , and Y_e define the number fraction of neutron, proton, and electron. For completely dissociated matter, the nucleon fractions are $Y_n = 1 Y_e$, and $Y_p = Y_e$.

APPENDIX E: SHEAR VISCOSITY COMPARISON

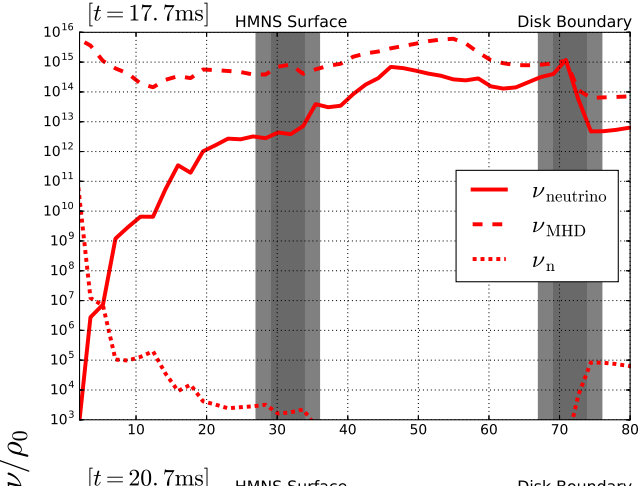
As suggested by Ref. [44], the diffusion of neutrinos trapped inside a HMNS can induce momentum transport, acting like an effective shear viscosity on length scales longer than the neutrino mean free path. In addition, if the neutrino mean free path is longer than the MRI wavelength, neutrinos induce a drag on the velocity field due to the Doppler effect between the fluid motion and the background radiation field [171,172]. According to Ref. [127], the effective viscosity and drag from neutrinos may then have a significant impact on the MRI inside a HMNS if magnetic fields are weaker than 10¹⁴ G. However, highresolution simulations of NSNS mergers have shown that seed magnetic fields can be boosted from ~1011 G to $\sim 10^{16}$ G within the first ~ 5 ms following merger (see, e.g., Refs. [15,104,128]). Therefore, the viscous effect on MRI due to neutrinos may be neglected. To assess the effect of neutrino momentum transport in our simulations, we compute the effective neutrino viscosity using the approximate analytical expression as in [173]

$$\begin{split} \nu_{\rm neutrino} &= 3.8 \times 10^{22} \\ &\times \left(\frac{T}{1\,{\rm MeV}}\right)^2 \left(\frac{\rho_0}{2.8 \times 10^{14}\,{\rm g\,cm^{-3}}}\right)^{-1} {\rm g\,cm^{-1}\,s^{-1}}, \end{split} \tag{E1}$$

which considers six species of nondegenerate neutrinos in local thermodynamic equilibrium and takes neutrino scattering as the dominant source of opacity. For the effective magnetic turbulent viscosity induced by MHD turbulence, we adopt the shear viscosity of an " α -disk" model [133,134],

$$\nu_{\text{MHD}} = \frac{2}{3} \frac{P}{\rho_0} \alpha_{\text{SS}} \Omega^{-1}, \tag{E2}$$

where $\alpha_{\rm SS}$ is the Shakura-Sunyaev stress parameter (see Sec. III E) and Ω is the characteristic angular frequency of the HMNS. Figure 13 displays $\nu_{\rm neutrino}$ and $\nu_{\rm MHD}$ as functions of radius along the x-axis Mag + Rad-Full by solid and dashed curves, respectively. Note that $\nu_{\rm MHD}$ is computed using an averaged value of $\alpha_{\rm SS} \sim 0.1$. The gray vertical regions span the approximate radii of the HMNS surface and disk outer boundary. Top and bottom panels show their behaviors at $t \sim 18$ ms (or $\sim 0.5 \tau_{\rm HMNS}$; see Table II) and $t \sim 21$ ms (just after BH formation),



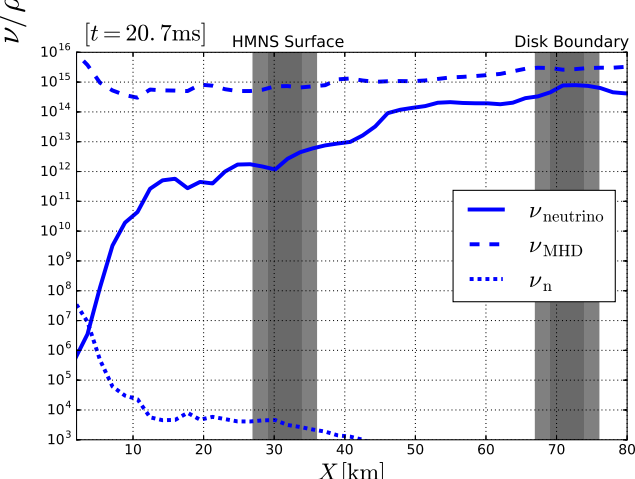


FIG. 13. Effective shear viscosity ν/ρ_0 due to neutrinos (solid curves), MHD turbulence (dashed curves), and nuclear interactions (dotted curves) along the *x*-axis Mag + Rad-Full during the HMNS (top panel) and BH + disk (bottom panel) phases. The gray vertical regions mark the approximate HMNS surface and disk outer boundary, respectively.

respectively. We find that $\nu_{\rm MHD}$ is a factor of $\gtrsim 10$ larger than $\nu_{\rm neutrino}$ inside the bulk of the HMNS. Therefore, we conclude that neutrino effective viscosity due to diffusion can be ignored whenever the magnetic field strength is $\gtrsim 10^{14}$ G, as is the case here. We evaluate the effect of viscosity on the linear growth of the MRI using the viscous Elsasser number $E_{\nu} \equiv v_A^2/(\nu_{\rm neutrino}\Omega)$ [44,135,136], which needs to be smaller than 1 for the effective neutrino viscosity to significantly affect the MRI growth. Using the average value of Alfvén speed and angular frequency in our cases, we find that $E_{\nu} > 10^4$ inside the HMNS and $E_{\nu} > 10^2$ in the disk. We also evaluate the critical field strength below which neutrino viscous effects become important [44], scaled to typical parameters inside our HMNS:

$$B_{\text{crit}} = 3.1 \times 10^{13} \left(\frac{\rho_0}{2.8 \times 10^{14} \,\text{g cm}^{-3}} \right) \times \left(\frac{\nu_{\text{neutrino}}}{3.8 \times 10^{22} \,\text{g cm}^{-1} \,\text{s}^{-1}} \right)^{1/2} \left(\frac{\Omega}{10^4 \,\text{s}^{-1}} \right)^{1/2} \,\text{G.} \quad (E3)$$

We find $B_{\rm crit}$ is at least a factor of 100 smaller than the typical field strength in the HMNS remnant (see Sec. IV). Similarly, the growth rate of MRI is hardly affected by the neutrino drag. As the neutrino drag can only be induced if the wavelength of the fastest growing MRI mode is shorter than the neutrino mean free path, there exists an upper limit of the magnetic field strength which cannot exceed ~10¹⁴ G in the HMNS remnant because $\lambda_{\rm MRI}$ is proportional to the magnetic field strength [44,127]. Note that from Ref. [127] neutrino drag is only important inside the HMNS but not in the disk, where the drag damping rate is smaller than the angular frequency. Therefore, we conclude that the effective viscosity due to MHD turbulence dominates over that induced by neutrino radiation in our simulations.

We also consider the microscopic shear viscosity of nucleon matter in the cores of the HMNS, which, for nonsuperfluid matter, is dominated by neutron-neutron and neutron-proton scattering mediated by strong interactions [174]. Note that the temperatures of interest in our models are mostly greater than the critical temperature $T \sim 10^{8-10}$ K below which dripped neutrons are likely to form Cooper pairs and undergo phase transitions to superfluid [175,176]. The shear viscosity due to in-vacuum nucleon-nucleon scattering in the nonsuperfluid liquid core was first estimated by Refs. [177,178], and an approximate and widely used fitting formula is given by Ref. [137]

$$\begin{split} \nu_n &= 8.2 \times 10^{14} \\ &\quad \times \left(\frac{T}{1\,\mathrm{MeV}}\right)^2 \left(\frac{\rho_0}{2.8 \times 10^{14}\,\mathrm{g\,cm^{-3}}}\right)^{9/4} \mathrm{g\,cm^{-1}\,s^{-1}}. \quad (E4) \end{split}$$

Another possible contribution to the shear viscosity comes from the collision of electrons and muons. According to Ref. [178], the shear viscosity is dominated by neutrons in

nonsuperfluid matter. Therefore, we ignore the effects from electrons and muons.

In Fig. 13, the dotted curves represent the viscosity due to the nucleon processes above using Eq. (E4). Near the core of the HMNS, the microscopic shear viscosity is comparable to ν_n . Nevertheless, at radius greater than 5 km, it quickly diminishes and becomes negligibly small compared to $\nu_{\rm MHD}$ and $\nu_{\rm n}$. Therefore, in our simulations, the shear viscosity due to nucleon scattering is minuscule and can be ignored as well. We again note that although the bulk viscosity has larger magnitude, the nucleon shear viscosity is most important during the inspiral and does not redistribute angular momentum in the remnant. It is the shear viscosity, which helps drive the HMNS to collapse and drives disk accretion onto the remnant BH. To conclude, the viscous effects due to neutrino diffusion, drag, and nucleon-nucleon scattering are small compared to the MHD turbulence in our systems.

APPENDIX F: CODE TEST—HEATED OPPENHEIMER-SNYDER COLLAPSE

1. General description

Here, we summarize results from one important test of our radiative transport scheme in a strong gravitational field. Other tests, including those involving shocks, have been previously performed in Ref. [80] and reproduced here. The collapse of a general relativistic, homogeneous, and pressureless sphere is given by the analytic Oppenheimer-Snyder (OS) solution [179]. We consider a thermal radiation perturbation to OS collapse in Ref. [180], in which the radiation is treated in the relativistic, thermal diffusion approximation for an optically thick radiation field that remains dynamically unimportant to the spacetime and collapsing dust sphere and where LTE is maintained throughout the collapse. The solution for the interior radiation field and outgoing flux as a function of radius and time were determined analytically in this case (see also Exercise 5.20 in Ref. [181]). In Ref. [182], we solved the full Boltzmann radiative transfer equation coupled to the radiation moment equations numerically to obtain the exact interior radiation intensity and flux for both optically thick and thin cases. The two methods showed close agreement in the optically thick limit. In Ref. [80], we again performed numerical simulations of "Heated OS collapse," now with the radiative transfer module in our Illinois GRMHD code. constrained to the optically thick limit. Again, the results closely matched the analytic solution. Recently, we carried out a similar treatment using a two-moment radiation transport scheme in the reference-metric formalism, again for an optically thick radiation field [84] in spherical symmetry. To test the reliability of our M1 implementation here, we again simulate heated OS collapse. For the first time, we not only treat the radiation field in the optically thick interior but also the outgoing field in the vacuum exterior, which is optically thin.

In our test, we set the initial areal radius $R_0 = 10M$, from which the initial rest-mass density $\rho_{0,\text{ini}} = 2.39 \times 10^{-4} M^{-2}$. We set $P_{0,\rm ini}=10^{-6}\rho_{0,\rm ini}$ to make matter pressure dynamically unimportant and $E_{0,\rm ini}=10^{-5}\rho_{0,\rm ini}$ to make radiation pressure unimportant, to recover heated OS collapse. We also set $v_{\rm ini}^i = F_{\rm ini}^i = 0$. The temperature of the sphere is initially set by the LTE condition $E = aT^4$. We choose the gray absorption opacity by setting the initial optical depth $\tau^a = R\kappa^a \rho_0 = 25$ and set the scattering opacity κ^s to zero. During collapse, the interior remains optically thick as the density increases with R^{-3} . We construct the initial metric based on the analytical OS solution, which matches a closed-Friedmann interior to the Schwarzschild exterior [183]. To be consistent with previous work, we adopt the hyperbolic driver conditions for the lapse and shift functions (see Eqs. (17) and (18) in Ref. [80]) with the same choice of freely specifiable constants a_1 , a_2 , a_3 , b_1 , and b_2 . Our grid consists of four nested refinement boxes centered in the sphere, with adjacent levels differing in size and resolution by factors of 2. The outer boundary is at $x_{\text{max}} = 60M$ and dx = 0.12M on the coarsest level. We note that the sphere is initially resolved by ≈2167 grid points across the diameter on the four levels. We endow the initial exterior regions with a low-density atmosphere with $\rho_{0,\mathrm{atm}}=10^{-12}\rho_{0,\mathrm{ini}}.$ To track both the interior and exterior evolution, we lift the "zero-temperature approximation" (E = 0) imposed by Refs. [84,180] at the stellar boundary and instead impose an outgoing radial radiation boundary condition in the near vacuum at the outer edge of our grid.

The profiles of rest-mass density, radiation energy density, and radiation flux as functions of radius at select moments of our heated OS collapse model are displayed in Fig. 14. The dotted and solid curves represent the numerical and analytical solutions, respectively. In the following sections, we describe our results and assess their reliability in regions with different optical thickness. We first compare our results in the optically thick region (stellar interior) with previous thermal OS collapse simulations using the Eddington closure schemes (with Eddington factor 1/3), and then we locate the photon trapping radius at the transition region and explain the behavior of radiation fields across it. Finally, we describe the free propagation of the radiation field in the optically thin exterior.

2. Optically thick region: Diffusion approximation

In Fig. 14, we show the comparisons of our numerical results computed using 50 Lagrangian fluid tracers for the rest-mass density ρ_0 (top panel), radiation energy density E (middle panel), and radiation flux scalar magnitude $F \equiv F^{\mu}F_{\mu}$ (bottom panel) with the analytic solutions

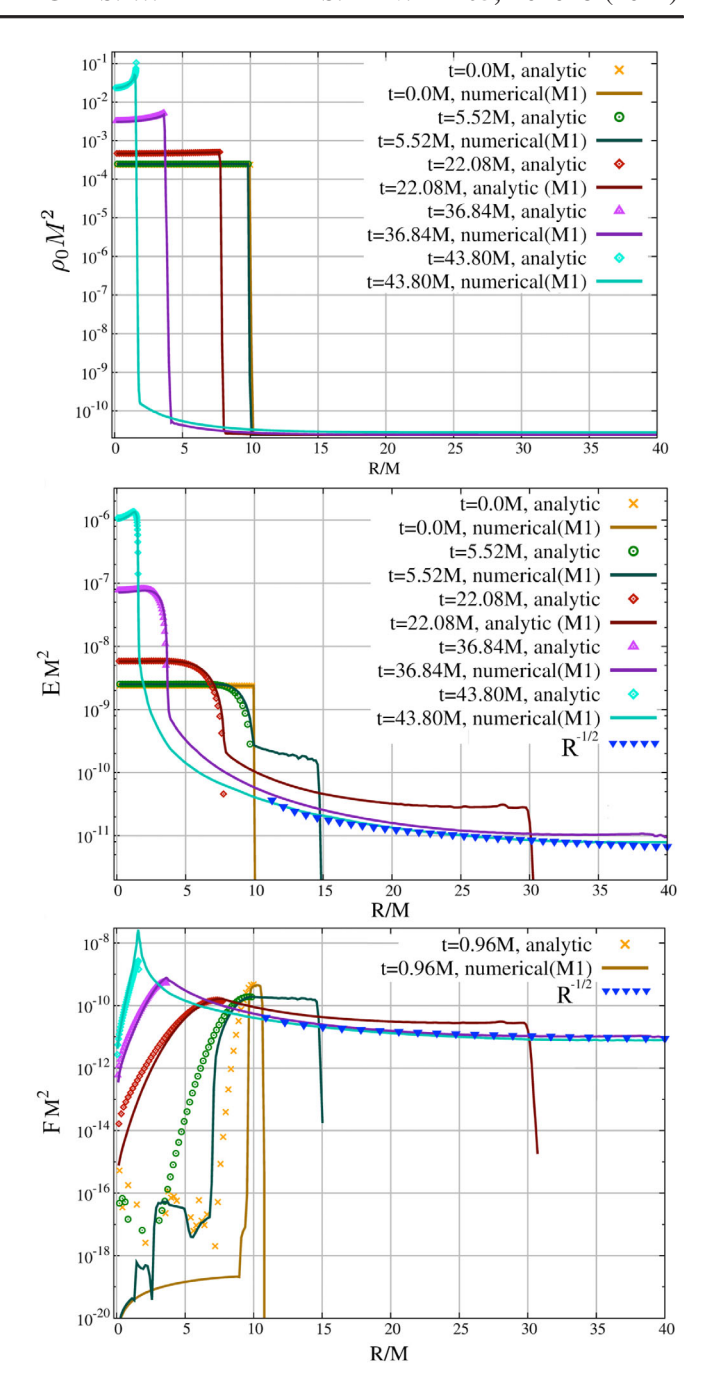


FIG. 14. Numerical (dotted curves) and analytical (solid curves) solutions at various times for the rest-mass density (top panel), radiation energy density E (middle panel), and radiation flux F (bottom panel) vs areal radius R for a heated OS collapse with initial areal radius $R_0 = 10$ M. The blue triangular dotted curve in the stellar exterior at the latest time represents the curve $\sim R^{-1/2}$.

summarized by Eqs. (D11)–(D13) in Ref. [80]. Our numerical solutions lie on top of the analytical ones in the stellar interior for the rest-mass density and radiation energy density (top and middle panels in Fig. 14). The radiation flux matches the analytical solution after the

initial transient phase (bottom panel in Fig. 14). Our numerical values also match the results in Ref. [84] in the stellar interior. Notice that we also recover the expected difference in F between the numerical and analytical results during the early phase of collapse, as reported and explained in Ref. [84] (which refers it as the "initial transient" phase). The difference originates from the computation of a (vanishingly) small quantity by subtracting two nearly equal quantities during the recovery of primitive variables in the region with a spatially nonconstant lapse. Nevertheless, at late stages, when the gauge and radiation characteristics have reached the stellar center, the numerical result of F becomes close to the analytical solution from the diffusion equation, as expected. Therefore, we conclude that the code reproduces the evolution of heated OS collapse consistent with previous works in the stellar interior (optically thick regions). Also, for this limit, our primitive solver matches the analytical expressions for the primitive variables (see Eqs. (65)–(67) in Ref. [80]) using Eddington closure.

3. Photon-trapping radius

According to Ref. [184], if the matter accretion rate is greater than $\dot{M}_{\rm E} \equiv L_{\rm E}/c^2$, where $L_{\rm E}$ is the Eddington limit, there exists a surface at radius $r_{\rm trap}$ within which the radiation is trapped and eventually falls into the BH with the gas. This photon trapping radius $r_{\rm trap}$ is defined by setting the infall speed of the gas equal to the approximate outward diffusion speed of the radiation ($\sim c/\tau$). At this radius, the radiation momentum density changes its direction, from inward inside $r_{\rm trap}$ to outward outside.

To approximate r_{trap} in our OS collapse model, we compute the optical depth by integrating $\kappa^a \rho_0$ along the xaxis. The top panel of Fig. 15 shows the stellar dust velocity, the diffusion speed of the radiation, c/τ , and the radiation momentum density along the x-axis at t =36.84*M* (corresponding to the maroon curve in Fig. 14). From the plot, the intersection between the diffusion speed and the gas velocity is at around x = 3.2 M, which agrees with the location at which the radiation momentum density \bar{S}^x turns over. As shown in the bottom panel, \bar{S}^x becomes negative at radius smaller than 3.2 M, indicating the radiation field is trapped and falls inward following the collapse of the star. We define the position x = 3.2M, labeled by the magenta vertical line in Fig. 15, as the radius of photon trapping of the model. It is expected that the radius would move inward with time and eventually freeze at 2M at BH formation. The consistency between trapping radius and flux direction turnover provides another useful check on our code.

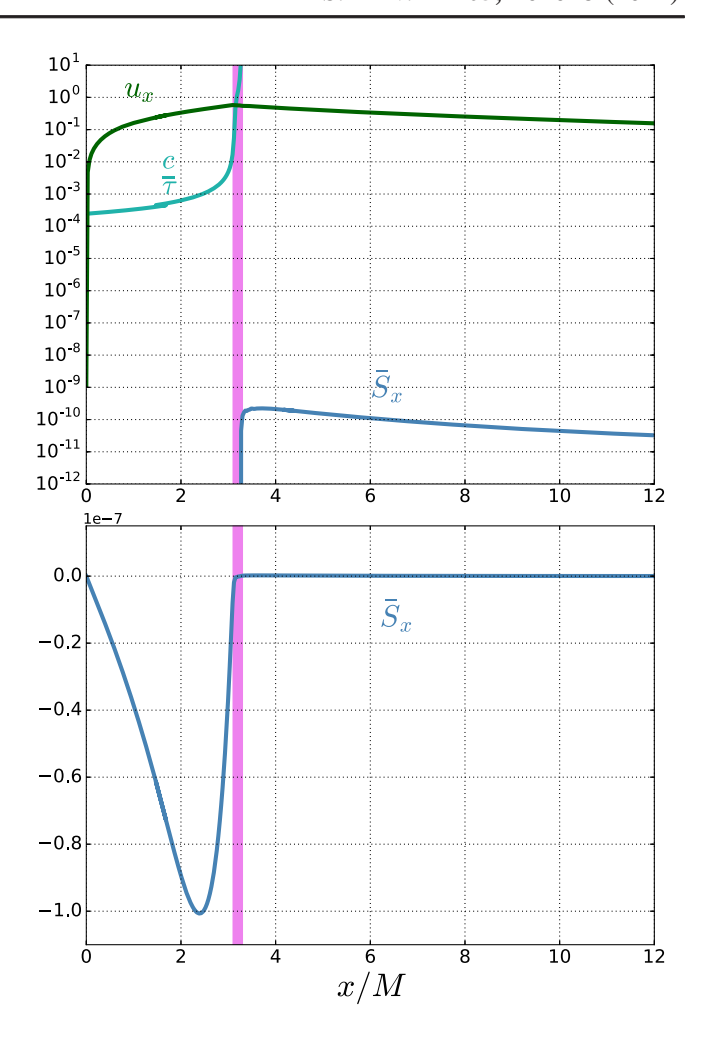


FIG. 15. Top panel: photon-trapping radius during OS collapse (magenta) where the radiation momentum density \bar{S}_x flips direction (blue). This radius can be also identified by equating the radius at which the gas velocity (green) equals the approximate radiation diffusion speed (cyan). Bottom panel: the change of sign (direction) of \bar{S}_x . Results are shown at t = 36.84M, when the areal surface of the star is at $R \approx 3.7M$.

4. Decay of radiation flux at large radius

With the M1 closure scheme of radiation, we are able to study radiation transport in the optically thin exterior region of the system. In the exterior, free propagation of radiation at the speed of light is expected. As shown in the middle and bottom panels of Fig. 14, the distance between the initial stellar surface at $R_0 = 10M$ and the radius marking the outermost nonzero E and F profiles approximates the time of evolution, indicating free propagation at the speed of light. At large radius, the magnitude of energy density equals that of the radiation flux E = F. This is confirmed in the two panels as well, where both E and F slowly fall together for radius R > 30M roughly as $R^{-1/2}$, as indicated

in Fig. 14. Note that as the star is collapsing the radiation source is not steady; therefore, the flux does not decay as R^{-2} as it would for a constant source.

One of the most important quantitative results is the exponential attenuation of the luminosity measured by a distant observer in the late stage of collapse, after the stellar surface has reached its gravitational radius at R = 2M [183,185,186]:

$$L_{\rm rad} \sim \exp\left(-\frac{t}{3\sqrt{3}M}\right).$$
 (F1)

The light is dominated by photons deposited in the unstable photon circular orbit at R=3M. They leak out at an exponential decay rate. To check our code, we perform a collapse model with the initial areal radius $R_{\rm ini}=4M$ and follow the collapse up to t=57M. This is approximately four times the collapse time, which is defined the time at which the stellar surface passes through an areal radius of R=2M for the first time. We fit our data for the flux F at R=23M from t=22M to t=56M with the exponential expression

$$F \to \exp(-t/t_1),$$
 (F2)

where t_1 is constant. We find that $t_1/M = 5.15^{+0.18}_{-0.17}$. Comparing with Eq. (F1), the fitted decay rate of the asymptotic flux data has less than 1% deviation from the

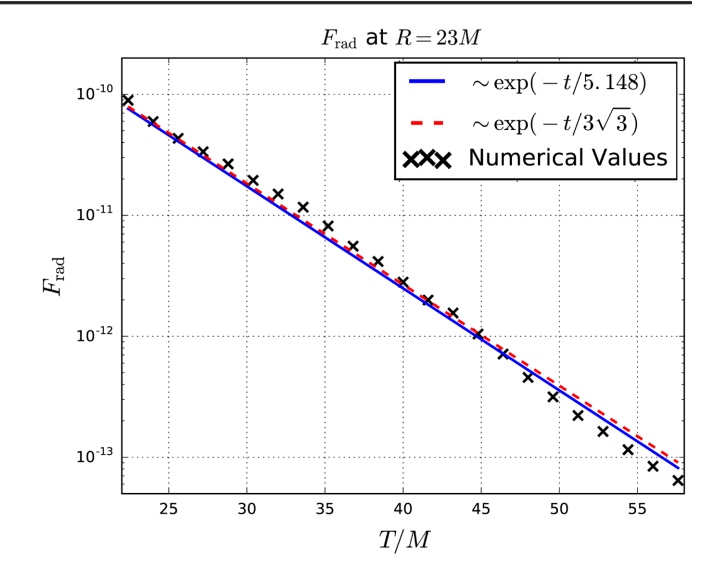


FIG. 16. The asymptotic scalar flux (black crosses), its best-fit line (blue), and the analytic curve Eq. (F1) (red) at R=23M at the late stage of collapse for the stellar model with the initial areal radius $R_{\rm ini}=4M$.

theoretic result, i.e., $t_1/M = 3\sqrt{3} \approx 5.20$. The corresponding plot is shown in Fig. 16. We conclude that the exponential decay of the asymptotic flux at large radius is correctly identified by our M1 code, showing its reliability in optically thin regions as well.

- [1] B. P. Abbott *et al.* (Virgo, LIGO Scientific Collaborations), Phys. Rev. Lett. **119**, 161101 (2017).
- [2] V. Savchenko et al., Astrophys. J. Lett. 848, L15 (2017).
- [3] P. S. Cowperthwaite *et al.*, Astrophys. J. Lett. **848**, L17 (2017).
- [4] M. Soares-Santos et al., Astrophys. J. Lett. 848, L16 (2017).
- [5] M. M. Kasliwal et al., Nature (London) 551, 75 (2017).
- [6] M. M. Kasliwal et al., Science 358, 1559 (2017).
- [7] R. Chornock et al., Astrophys. J. Lett. 848, L19 (2017).
- [8] B. P. Abbott *et al.* (Virgo, Fermi-GBM, INTEGRAL, LIGO Scientific Collaborations), Astrophys. J. **848**, L13 (2017).
- [9] A. von Kienlin, C. Meegan, and A. Goldstein, GRB 170817A: Fermi GBM detection, GRB Coordinates Network, Circular Service, No. 21520, #1 (2017) 1520 (2017), http://adsabs.harvard.edu/abs/2017GCN.21520....1V.
- [10] V. Savchenko et al., Astrophys. J. 848, L15 (2017).
- [11] S. Valenti, D. J. Sand, S. Yang, E. Cappellaro, L. Tartaglia, A. Corsi, S. W. Jha, D. E. Reichart, J. Haislip, and V. Kouprianov, Astrophys. J. Lett. 848, L24 (2017).
- [12] M. Obergaulinger, M. A. Aloy, and E. Müller, Astron. Astrophys. **515**, A30 (2010).

- [13] J. Zrake and A. I. MacFadyen, Astrophys. J. **769**, L29 (2013).
- [14] K. Kiuchi, P. Cerdá-Durán, K. Kyutoku, Y. Sekiguchi, and M. Shibata, Phys. Rev. D 92, 124034 (2015).
- [15] C. Palenzuela, R. Aguilera-Miret, F. Carrasco, R. Ciolfi, J. V. Kalinani, W. Kastaun, B. Miñano, and D. Viganò, arXiv:2112.08413.
- [16] D. M. Siegel, R. Ciolfi, and L. Rezzolla, Astrophys. J. 785, L6 (2014).
- [17] K. Kiuchi, Y. Sekiguchi, K. Kyutoku, and M. Shibata, Classical Quantum Gravity **29**, 124003 (2012).
- [18] D. J. Price and S. Rosswog, Science **312**, 719 (2006).
- [19] M. D. Duez, Y. T. Liu, S. L. Shapiro, M. Shibata, and B. C. Stephens, Phys. Rev. D 73, 104015 (2006).
- [20] M. Anderson, E. W. Hirschmann, L. Lehner, S. L. Liebling, P. M. Motl, D. Neilsen, C. Palenzuela, and J. E. Tohline, Phys. Rev. Lett. 100, 191101 (2008).
- [21] L. Rezzolla, B. Giacomazzo, L. Baiotti, J. Granot, C. Kouveliotou, and M. A. Aloy, Astrophys. J. Lett. 732, L6 (2011).
- [22] B. Giacomazzo, L. Rezzolla, and L. Baiotti, Phys. Rev. D 83, 044014 (2011).

- [23] K. Dionysopoulou, D. Alic, C. Palenzuela, L. Rezzolla, and B. Giacomazzo, Phys. Rev. D 88, 044020 (2013).
- [24] D. Neilsen, S. L. Liebling, M. Anderson, L. Lehner, E. O'Connor, and C. Palenzuela, Phys. Rev. D 89, 104029 (2014).
- [25] C. Palenzuela, S. L. Liebling, D. Neilsen, L. Lehner, O. L. Caballero, E. O'Connor, and M. Anderson, Phys. Rev. D 92, 044045 (2015).
- [26] M. Ruiz, R. N. Lang, V. Paschalidis, and S. L. Shapiro, Astrophys. J. 824, L6 (2016).
- [27] R. Ciolfi, W. Kastaun, J. V. Kalinani, and B. Giacomazzo, Phys. Rev. D 100, 023005 (2019).
- [28] M. Ruiz, A. Tsokaros, V. Paschalidis, and S. L. Shapiro, Phys. Rev. D 99, 084032 (2019).
- [29] R. Ciolfi, Mon. Not. R. Astron. Soc. 495, L66 (2020).
- [30] R. Aguilera-Miret, D. Viganò, and C. Palenzuela, Astrophys. J. Lett. 926, L31 (2022).
- [31] R. D. Blandford and R. L. Znajek, Mon. Not. R. Astron. Soc. 179, 433 (1977).
- [32] M. Ruiz, S. L. Shapiro, and A. Tsokaros, Phys. Rev. D **98**, 123017 (2018).
- [33] M. Ruiz, A. Tsokaros, and S. L. Shapiro, Phys. Rev. D 101, 064042 (2020).
- [34] V. Paschalidis, M. Ruiz, and S. L. Shapiro, Astrophys. J. **806**, L14 (2015).
- [35] R. Popham, S. E. Woosley, and C. Fryer, Astrophys. J. **518**, 356 (1999).
- [36] T. Di Matteo, R. Perna, and R. Narayan, Astrophys. J. 579, 706 (2002).
- [37] W.-H. Lei, B. Zhang, and E.-W. Liang, Astrophys. J. 765, 125 (2013).
- [38] O. Just, M. Obergaulinger, H.-T. Janka, A. Bauswein, and N. Schwarz, Astrophys. J. Lett. 816, L30 (2016).
- [39] S. Rosswog and E. Ramirez-Ruiz, Mon. Not. R. Astron. Soc. 343, L36 (2003).
- [40] L. Dessart, C. D. Ott, A. Burrows, S. Rosswog, and E. Livne, Astrophys. J. 690, 1681 (2009).
- [41] A. Perego, S. Rosswog, R. M. Cabezón, O. Korobkin, R. Käppeli, A. Arcones, and M. Liebendörfer, Mon. Not. R. Astron. Soc. 443, 3134 (2014).
- [42] A. Murguia-Berthier, E. Ramirez-Ruiz, F. D. Colle, A. Janiuk, S. Rosswog, and W. H. Lee, Astrophys. J. **908**, 152 (2021).
- [43] W.-H. Lei, B. Zhang, X.-F. Wu, and E.-W. Liang, Astrophys. J. **849**, 47 (2017).
- [44] J. Guilet, E. Müller, and H.-T. Janka, Mon. Not. R. Astron. Soc. **447**, 3992 (2015).
- [45] F. F. Dirirsa, Proc. Sci. HEASA2016 (2017) 004, https://ui.adsabs.harvard.edu/abs/2016heas.confE...4D.
- [46] Y. Sekiguchi, Classical Quantum Gravity 27, 114107 (2010).
- [47] M. B. Deaton, M. D. Duez, F. Foucart, E. O'Connor, C. D. Ott, L. E. Kidder, C. D. Muhlberger, M. A. Scheel, and B. Szilagyi, Astrophys. J. 776, 47 (2013).
- [48] M. Shibata, K. Kiuchi, Y. Sekiguchi, and Y. Suwa, Prog. Theor. Phys. 125, 1255 (2011).
- [49] S. Wanajo, Y. Sekiguchi, N. Nishimura, K. Kiuchi, K. Kyutoku, and M. Shibata, Astrophys. J. 789, L39 (2014).

- [50] F. Foucart, E. O'Connor, L. Roberts, M. D. Duez, R. Haas, L. E. Kidder, C. D. Ott, H. P. Pfeiffer, M. A. Scheel, and B. Szilagyi, Phys. Rev. D 91, 124021 (2015).
- [51] S. Fujibayashi, S. Wanajo, K. Kiuchi, K. Kyutoku, Y. Sekiguchi, and M. Shibata, Astrophys. J. **901**, 122 (2020).
- [52] D. Radice, F. Galeazzi, J. Lippuner, L. F. Roberts, C. D. Ott, and L. Rezzolla, Mon. Not. R. Astron. Soc. 460, 3255 (2016).
- [53] F. Foucart, E. O'Connor, L. Roberts, L. E. Kidder, H. P. Pfeiffer, and M. A. Scheel, Phys. Rev. D 94, 123016 (2016).
- [54] F. Foucart, M. D. Duez, F. Hebert, L. E. Kidder, H. P. Pfeiffer, and M. A. Scheel, Astrophys. J. 902, L27 (2020).
- [55] F. Foucart, M. D. Duez, F. Hébert, L. E. Kidder, P. Kovarik, H. P. Pfeiffer, and M. A. Scheel, Astrophys. J. 920, 82 (2021).
- [56] P. Mösta, D. Radice, R. Haas, E. Schnetter, and S. Bernuzzi, Astrophys. J. 901, L37 (2020).
- [57] Y.-C. Zou and T. Piran, Mon. Not. R. Astron. Soc. 402, 1854 (2010).
- [58] K. Hayashi, S. Fujibayashi, K. Kiuchi, K. Kyutoku, Y. Sekiguchi, and M. Shibata, arXiv:2111.04621.
- [59] F. Douchin and P. Haensel, Astron. Astrophys. 380, 151 (2001).
- [60] P. Beniamini, R. B. Duran, M. Petropoulou, and D. Giannios, Astrophys. J. 895, L33 (2020).
- [61] P. Narayana Bhat et al., Astrophys. J. Suppl. Ser. 223, 28 (2016).
- [62] A. Lien, T. Sakamoto, S. D. Barthelmy, W. H. Baumgartner, J. K. Cannizzo, K. Chen, N. R. Collins, J. R. Cummings, N. Gehrels, H. A. Krimm, C. B. Markwardt, D. M. Palmer, M. Stamatikos, E. Troja, and T. N. Ukwatta, Astrophys. J. 829, 7 (2016).
- [63] Z. B. Etienne, J. A. Faber, Y. T. Liu, S. L. Shapiro, K. Taniguchi, and T. W. Baumgarte, Phys. Rev. D 77, 084002 (2008).
- [64] Z. B. Etienne, V. Paschalidis, and S. L. Shapiro, Phys. Rev. D 86, 084026 (2012).
- [65] R. Gold, V. Paschalidis, Z. B. Etienne, S. L. Shapiro, and H. P. Pfeiffer, Phys. Rev. D 89, 064060 (2014).
- [66] A. Tsokaros, M. Ruiz, V. Paschalidis, S. L. Shapiro, and K. Uryū, Phys. Rev. D 100, 024061 (2019).
- [67] A. Tsokaros, M. Ruiz, S. L. Shapiro, L. Sun, and K. b. o. Uryū, Phys. Rev. Lett. 124, 071101 (2020).
- [68] M. Ruiz, V. Paschalidis, A. Tsokaros, and S. L. Shapiro, Phys. Rev. D 102, 124077 (2020).
- [69] Y. T. Liu, S. L. Shapiro, Z. B. Etienne, and K. Taniguchi, Phys. Rev. D 78, 024012 (2008).
- [70] Z. B. Etienne, Y. T. Liu, and S. L. Shapiro, Phys. Rev. D 82, 084031 (2010).
- [71] Cactus Development Team, Cactus, http://www.cactuscode.org (2010).
- [72] E. Schnetter, Carpet, http://www.cactuscode.org (2010).
- [73] M. Shibata and T. Nakamura, Phys. Rev. D 52, 5428 (1995).
- [74] T. W. Baumgarte and S. L. Shapiro, Phys. Rev. D 59, 024007 (1998).
- [75] J. G. Baker, J. Centrella, D.-I. Choi, M. Koppitz, and J. van Meter, Phys. Rev. Lett. 96, 111102 (2006).

- [76] M. Campanelli, C. O. Lousto, P. Marronetti, and Y. Zlochower, Phys. Rev. Lett. 96, 111101 (2006).
- [77] J. G. Baker, J. Centrella, D.-I. Choi, M. Koppitz, and J. van Meter, Phys. Rev. D 73, 104002 (2006).
- [78] Z. B. Etienne, V. Paschalidis, Y. T. Liu, and S. L. Shapiro, Phys. Rev. D 85, 024013 (2012).
- [79] B. D. Farris, R. Gold, V. Paschalidis, Z. B. Etienne, and S. L. Shapiro, Phys. Rev. Lett. 109, 221102 (2012).
- [80] B. D. Farris, T. K. Li, Y. T. Liu, and S. L. Shapiro, Phys. Rev. D 78, 024023 (2008).
- [81] Z. B. Etienne, Y. T. Liu, V. Paschalidis, and S. L. Shapiro, Phys. Rev. D 85, 064029 (2012).
- [82] K. S. Thorne, Mon. Not. R. Astron. Soc. 194, 439 (1981).
- [83] G. N. Minerbo, J. Quant. Spectrosc. Radiat. Transfer 20, 541 (1978).
- [84] T. W. Baumgarte and S. L. Shapiro, Phys. Rev. D 102, 104001 (2020).
- [85] C. Y. Cardall, E. Endeve, and A. Mezzacappa, Phys. Rev. D 87, 103004 (2013).
- [86] M. Ruffert, H. T. Janka, and G. Schaefer, Astron. Astrophys. 311, 532 (1996), https://ui.adsabs.harvard.edu/abs/1996A&A...311..532R.
- [87] A. Burrows, T. Young, P. Pinto, R. Eastman, and T. A. Thompson, Astrophys. J. 539, 865 (2000).
- [88] K. Takahashi, M. F. El Eid, and W. Hillebrandt, Astron. Astrophys. **67**, 185 (1978), https://ui.adsabs.harvard.edu/abs/1978A&A....67..185T.
- [89] M. D. Duez, Y. T. Liu, S. L. Shapiro, and B. C. Stephens, Phys. Rev. D 72, 024028 (2005).
- [90] J. S. Read, B. D. Lackey, B. J. Owen, and J. L. Friedman, Phys. Rev. D 79, 124032 (2009).
- [91] T. Fischer, Astron. Astrophys. 593, A103 (2016).
- [92] W. D. Arnett, Astrophys. J. 218, 815 (1977).
- [93] D. L. Tubbs, T. A. Weaver, R. L. Bowers, J. R. Wilson, and D. N. Schramm, Astrophys. J. 239, 271 (1980).
- [94] A. Tsokaros, K. Uryū, and L. Rezzolla, Phys. Rev. D 91, 104030 (2015).
- [95] A. Tsokaros, K. Uryu, M. Ruiz, and S. L. Shapiro, Phys. Rev. D 98, 124019 (2018).
- [96] M. Ruiz, A. Tsokaros, and S. L. Shapiro, Phys. Rev. D 104, 124049 (2021).
- [97] T. E. Riley et al., Astrophys. J. Lett. 918, L27 (2021).
- [98] E. Fonseca et al., Astrophys. J. 832, 167 (2016).
- [99] J. Antoniadis et al., Science **340**, 6131 (2013).
- [100] H. T. Cromartie *et al.* (NANOGrav Collaboration), Nat. Astron. **4**, 72 (2020).
- [101] P. T. H. Pang, I. Tews, M. W. Coughlin, M. Bulla, C. Van Den Broeck, and T. Dietrich, Astrophys. J. **922**, 14 (2021).
- [102] B. P. Abbott *et al.* (LIGO Scientific, Virgo Collaborations), Phys. Rev. Lett. **121**, 161101 (2018).
- [103] M. Ruiz and S. L. Shapiro, Phys. Rev. D **96**, 084063 (2017).
- [104] R. Aguilera-Miret, D. Viganò, F. Carrasco, B. Miñano, and C. Palenzuela, Phys. Rev. D **102**, 103006 (2020).
- [105] K. Fujikawa and R. E. Shrock, Phys. Rev. Lett. 45, 963 (1980).
- [106] C.-S. Lim and W. J. Marciano, Phys. Rev. D 37, 1368 (1988).
- [107] A. Vlasenko, G. M. Fuller, and V. Cirigliano, Phys. Rev. D 89, 105004 (2014).

- [108] B. van Leer, J. Comput. Phys. 23, 276 (1977).
- [109] W. H. Press, S. A. Teukolsky, W. T. Vetterling, and B. P. Flannery, *Numerical Recipes in C. The Art of Scientific Computing* (Cambridge University Press, Cambridge, 1992), https://ui.adsabs.harvard.edu/abs/1992nrca.book.... P.
- [110] J. Thornburg, Classical Quantum Gravity 21, 743 (2004).
- [111] O. Dreyer, B. Krishnan, D. Shoemaker, and E. Schnetter, Phys. Rev. D 67, 024018 (2003).
- [112] M. Ruiz, M. Alcubierre, D. Núñez, and R. Takahashi, Gen. Relativ. Gravit. 40, 1705 (2008).
- [113] B. D. Farris, Y. T. Liu, and S. L. Shapiro, Phys. Rev. D 81, 084008 (2010).
- [114] Z. B. Etienne, Y. T. Liu, V. Paschalidis, and S. L. Shapiro, Phys. Rev. D 85, 064029 (2012).
- [115] T. Sano, S.-i. Inutsuka, N. J. Turner, and J. M. Stone, Astrophys. J. 605, 321 (2004).
- [116] H. Shiokawa, J. C. Dolence, C. F. Gammie, and S. C. Noble, Astrophys. J. 744, 187 (2012).
- [117] N. I. Shakura and R. A. Sunyaev, Astron. Astrophys. 24, 337 (1973), https://ui.adsabs.harvard.edu/abs/1973A&A... 24..337S.
- [118] R. F. Penna, J. C. McKinney, R. Narayan, A. Tchekhovskoy, R. Shafee, and J. E. McClintock, Mon. Not. R. Astron. Soc. 408, 752 (2010).
- [119] D. Radice, A. Perego, K. Hotokezaka, S. A. Fromm, S. Bernuzzi, and L. F. Roberts, Astrophys. J. 869, 130 (2018).
- [120] D. Radice, S. Bernuzzi, A. Perego, and R. Haas, Mon. Not. R. Astron. Soc. 512, 1499 (2022).
- [121] L.-X. Li and B. Paczynski, Astrophys. J. Lett. 507, L59 (1998).
- [122] B. D. Metzger, Living Rev. Relativity 20, 3 (2017).
- [123] L. D. Matthews et al., Publ. Astron. Soc. Pac. 130, 015002 (2018).
- [124] H.-Y. Chen, P. S. Cowperthwaite, B. D. Metzger, and E. Berger, Astrophys. J. Lett. **908**, L4 (2021).
- [125] S. L. Shapiro, Astrophys. J. 544, 397 (2000).
- [126] L. Sun, M. Ruiz, and S. L. Shapiro, Phys. Rev. D **99**, 064057 (2019).
- [127] J. Guilet, A. Bauswein, O. Just, and H.-T. Janka, Mon. Not. R. Astron. Soc. 471, 1879 (2017).
- [128] K. Kiuchi, K. Kyutoku, Y. Sekiguchi, M. Shibata, and T. Wada, Phys. Rev. D 90, 041502 (2014).
- [129] M. Ruiz, A. Tsokaros, V. Paschalidis, and S. L. Shapiro, Phys. Rev. D 99, 084032 (2019).
- [130] K. Kiuchi, K. Kyutoku, Y. Sekiguchi, and M. Shibata, Phys. Rev. D 97, 124039 (2018).
- [131] V. Paschalidis, W. E. East, F. Pretorius, and S. L. Shapiro, Phys. Rev. D 92, 121502 (2015).
- [132] W. E. East, V. Paschalidis, F. Pretorius, and S. L. Shapiro, Phys. Rev. D 93, 024011 (2016).
- [133] P. Artymowicz and S. H. Lubow, Astrophys. J. **421**, 651 (1994).
- [134] A. I. MacFadyen and M. Milosavljević, Astrophys. J. 672, 83 (2008).
- [135] M. E. Pessah and C. kwan Chan, Astrophys. J. **684**, 498 (2008).
- [136] P.-Y. Longaretti and G. Lesur, Astron. Astrophys. 516, A51 (2010).
- [137] C. Cutler and L. Lindblom, Astrophys. J. **314**, 234 (1987).

- [138] E. R. Most, S. P. Harris, C. Plumberg, M. G. Alford, J. Noronha, J. Noronha-Hostler, F. Pretorius, H. Witek, and N. Yunes, Mon. Not. R. Astron. Soc. 509, 1096 (2021).
- [139] P. N. Bhat et al., Astrophys. J. Suppl. Ser. 223, 28 (2016).
- [140] P. Beniamini, R. B. Duran, M. Petropoulou, and D. Giannios, Astrophys. J. Lett. 895, L33 (2020).
- [141] S. L. Shapiro, Phys. Rev. D 95, 101303 (2017).
- [142] Y. Li, B. Zhang, and H.-J. Lü, Astrophys. J. Suppl. Ser. 227, 7 (2016).
- [143] K. S. Thorne, R. H. Price, and D. A. Macdonald, *The Membrane Paradigm* (Yale University Press, New Haven, 1986).
- [144] S. S. Komissarov, Mon. Not. R. Astron. Soc. **326**, L41 (2001).
- [145] B. P. Abbott *et al.* (LIGO Scientific Collaboration), Classical Quantum Gravity **34**, 044001 (2017).
- [146] A. Bauswein and N. Stergioulas, Phys. Rev. D 91, 124056 (2015).
- [147] S. Vretinaris, N. Stergioulas, and A. Bauswein, Phys. Rev. D 101, 084039 (2020).
- [148] K. Takami, L. Rezzolla, and L. Baiotti, Phys. Rev. Lett. 113, 091104 (2014).
- [149] K. Takami, L. Rezzolla, and L. Baiotti, Phys. Rev. D 91, 064001 (2015).
- [150] L. Rezzolla and K. Takami, Phys. Rev. D 93, 124051 (2016).
- [151] N. Stergioulas, A. Bauswein, K. Zagkouris, and H.-T. Janka, Mon. Not. R. Astron. Soc. 418, 427 (2011).
- [152] S. Hild *et al.*, Classical Quantum Gravity **28**, 094013 (2011).
- [153] B. Allen, W. G. Anderson, P. R. Brady, D. A. Brown, and J. D. E. Creighton, Phys. Rev. D 85, 122006 (2012).
- [154] I. Harry and T. Hinderer, Classical Quantum Gravity 35, 145010 (2018).
- [155] D. Shoemaker, LIGO Report No. LIGO-T0900288-v2, 2009, the high-power detuned model used in this paper is given in the data file, ZERO_DET_HIGH_Pxf.TXT.
- [156] T. W. Baumgarte and S. L. Shapiro, Astrophys. J. 504, 431 (1998).
- [157] Y. Sekiguchi, K. Kiuchi, K. Kyutoku, M. Shibata, and K. Taniguchi, Phys. Rev. D **93**, 124046 (2016).
- [158] J. M. Lattimer and D. F. Swesty, Nucl. Phys. **A535**, 331 (1991).
- [159] H. Shen, H. Toki, K. Oyamatsu, and K. Sumiyoshi, Nucl. Phys. A637, 435 (1998).
- [160] M. Hempel and J. Schaffner-Bielich, Nucl. Phys. A837, 210 (2010).
- [161] F. Foucart, M. D. Duez, L. E. Kidder, R. Nguyen, H. P. Pfeiffer, and M. A. Scheel, Phys. Rev. D 98, 063007 (2018).

- [162] T. W. Baumgarte, S. L. Shapiro, and S. A. Teukolsky, Astrophys. J. 458, 680 (1996).
- [163] C. F. Gammie, J. C. McKinney, and G. Toth, Astrophys. J. 589, 444 (2003).
- [164] S. C. Noble, C. F. Gammie, J. C. McKinney, and L. D. Zanna, Astrophys. J. 641, 626 (2006).
- [165] Z. B. Etienne, V. Paschalidis, R. Haas, P. Mosta, and S. L. Shapiro, Classical Quantum Gravity 32, 175009 (2015).
- [166] B. Giacomazzo and L. Rezzolla, Classical Quantum Gravity **24**, S235 (2007).
- [167] P. Mösta, B. C. Mundim, J. A. Faber, R. Haas, S. C. Noble, T. Bode, F. Löffler, C. D. Ott, C. Reisswig, and E. Schnetter, Classical Quantum Gravity 31, 015005 (2014).
- [168] S. C. Noble, J. H. Krolik, and J. F. Hawley, Astrophys. J. 692, 411 (2009).
- [169] S. L. Shapiro and S. A. Teukolsky, *Black Holes, White Dwarfs, and Neutron Stars: The Physics of Compact Objects* (Wiley-Interscience, New York, 1983).
- [170] S. W. Bruenn, Astrophys. J. Suppl. Ser. 58, 771 (1985).
- [171] E. Agol and J. Krolik, Astrophys. J. 507, 304 (1998).
- [172] K. Jedamzik, V. c. v. Katalinić, and A. V. Olinto, Phys. Rev. D 57, 3264 (1998).
- [173] W. Keil, H. T. Janka, and E. Mueller, Astrophys. J. Lett. 473, L111 (1996).
- [174] P. S. Shternin and D. G. Yakovlev, Phys. Rev. D 78, 063006 (2008).
- [175] A. Gezerlis, C. J. Pethick, and A. Schwenk, arXiv:1406.6109.
- [176] B. Bertoni, S. Reddy, and E. Rrapaj, Phys. Rev. C 91, 025806 (2015).
- [177] E. Flowers and N. Itoh, Astrophys. J. 206, 218 (1976).
- [178] E. Flowers and N. Itoh, Astrophys. J. 230, 847 (1979).
- [179] J. R. Oppenheimer and H. Snyder, Phys. Rev. 56, 455 (1939).
- [180] S. L. Shapiro, Phys. Rev. D 40, 1858 (1989).
- [181] T. W. Baumgarte and S. L. Shapiro, *Numerical Relativity: Solving Einstein's Equations on the Computer* (Cambridge University Press, Cambridge, England, 2010).
- [182] S. L. Shapiro, Astrophys. J. 472, 308 (1996).
- [183] C. W. Misner, K. S. Thorne, and J. A. Wheeler, *Gravitation* (Freeman, San Francisco, 1973).
- [184] M. C. Begelman, Mon. Not. R. Astron. Soc. **187**, 237 (1979).
- [185] M. A. Podurets, Sov. Astron. **8**, 868 (1965), https://ui.adsabs.harvard.edu/abs/1965SvA.....8..868P.
- [186] W. L. Ames and K. S. Thorne, Astrophys. J. **151**, 659 (1968).